The Astrophysical Journal, 688:418–436, 2008 November 20


# X-RAY FLARES IN ORION YOUNG STARS. I. FLARE CHARACTERISTICS

Konstantin V. Getman,[1] Eric D. Feigelson,[1] Patrick S. Broos,[1] Giuseppina Micela,[2] and Gordon P. Garmire[1]

*Received 2008 March 25; accepted 2008 July 11*


## ABSTRACT

Pre–main-sequence (PMS) stars are known to produce powerful X-ray flares, which resemble magnetic reconnection solar flares scaled by factors up to $10^4$. However, there are numerous puzzles, including the structure of X-ray-emitting coronae and magnetospheres, the effects of protoplanetary disks, and the effects of stellar rotation. To investigate these issues in detail, we examine 216 of the brightest flares from 161 PMS stars observed in the *Chandra* Orion Ultradeep Project (COUP). These constitute the largest homogeneous data set of PMS, or indeed stellar flares at any stellar age, ever acquired. Our effort is based on a new flare spectral analysis technique that avoids nonlinear parametric modeling. We provide a catalog of derived properties and an electronic atlas for this unique collection of flares. The current study (Paper I) examines the flare morphologies, and provides a general comparison of COUP flare characteristics with those of other active X-ray stars and the Sun. Paper II will concentrate on relationships between flare behavior, protoplanetary disks, and other stellar properties. Several results are obtained. First, COUP flares are among the most powerful, longest, and hottest, corresponding to the largest known coronal structures. Second, no significant statistical differences in peak flare luminosity or temperature distributions are found among different morphological flare classes, suggesting a common underlying mechanism for all flares. Third, comparison with the general solar scaling laws indicates that COUP flares may not adequately fit proposed power-temperature and duration-temperature solar-stellar fits. Fourth, COUP superhot flares are found to be brighter but shorter than cooler COUP flares. Finally, the majority of bright COUP flares can be viewed as enhanced analogs of the rare solar "long-duration events."


*Subject headings:* open clusters and associations: individual (Orion Nebula Cluster) — stars: flare — stars: pre–main-sequence — X-rays: stars

*Online material:* extended figure set, machine-readable tables

## 1. INTRODUCTION

All solar-type stars exhibit their highest levels of magnetic activity during their pre–main-sequence (PMS) phase (Feigelson et al. 2007). This includes "superflares" with peak luminosities $\log L_X \gtrsim 32$ erg s$^{-1}$ in the 0.5–8 keV band, $10^4$ more powerful than the strongest flares seen in the contemporary Sun (e.g., Tsuboi et al. 1998; Grosso et al. 2004; Favata et al. 2005). PMS stars thus join RS CVn binary systems (e.g., Osten et al. 2007) as laboratories to study the physics of the most powerful magnetic reconnection events. PMS stars are more distant and fainter than the closer RS CVn systems, but hundreds of flaring PMS stars can be simultaneously studied due to their concentration in rich clusters.

The magnetic field structure of PMS stars, and thus the nature of their reconnection and flaring, may (or may not) qualitatively differ from other stars due to the presence of a protoplanetary disk during the early PMS stages. The intense high-energy radiation from these PMS reconnection events may affect the physical and chemical properties of the surrounding circumstellar environment and play an important role in the formation of planets (Glassgold et al. 2005; Feigelson et al. 2007). A consensus has emerged during the past decade that PMS accretion is funneled by magnetic field lines linking the disk inner edge to the stellar surface (e.g., Hartmann 1998; Shu et al. 2000). However, while early theory assumed a dipolar field morphology, recent studies point to a complex multipolar field structure similar to the Sun's (Jardine et al. 2006; Donati et al. 2007; Long et al. 2008).

It is also unclear whether the X-ray flares occur primarily in large loops with both footprints anchored on the stellar surface, or in loops linking the stellar photosphere with the inner rim of the circumstellar disk (Isobe et al. 2003; Favata et al. 2005). The first case may suffer instability due to centrifugal force (Jardine & Unruh 1999), while the second case may load the loop with cool accreting material so that X-rays may not be produced (Preibisch et al. 2005).

The *Chandra* Orion Ultradeep Project (COUP; Getman et al. 2005b), a 13 day nearly continuous observation of ∼1408 PMS stars in the Orion Nebula, enables both studies of individual flare properties and statistical studies of flaring from Orion stars (Wolk et al. 2005; Flaccomio et al. 2005; Stassun et al. 2006; Caramazza et al. 2007; Albacete Colombo et al. 2007). COUP also provided a unique opportunity to study relatively rare superflares and long-duration flares. Favata et al. (2005) have analyzed the strongest 32 flares in the COUP data set using the establish method of time-resolved spectroscopy (TRS) modeled as cooling plasma loops. They concluded that at least 1/3 of these are produced by magnetic reconnection in very long coronal $5-20\,R_\star$ structures. Such structures were predicted in magnetospheric accretion models (e.g., Shu et al. 1997) but not clearly identified before COUP. Favata et al. (2005) recognized that their sample was too small to quantitatively probe the relationship between long coronal flaring structure and disks or accretion.

The aim of the current study is to extend the flare sample of Favata et al. (2005) utilizing a more sensitive technique of flare analysis, the "method of adaptively smoothed median energy" (MASME) introduced by Getman et al. (2006). We combine this method with the astrophysical cooling loop models of Reale et al. (1997) to trace the evolution of the flare plasma in temperature-density diagrams and derive flaring loop sizes. The method

[1] Department of Astronomy and Astrophysics, 525 Davey Laboratory, Pennsylvania State University, University Park, PA 16802; gkosta@astro.psu.edu.
[2] INAF, Osservatorio Astronomico di Palermo G. S. Vaiana, Piazza del Parlamento 1, I-90134 Palermo, Italy.

allowed us to examine 216 of the brightest flares from 161 of the brightest COUP PMS stars. These constitute the largest homogeneous sample of powerful stellar flares ever acquired in the X-ray band. In Paper II, we use these results to study in detail the relationships between PMS X-ray flares, stellar properties, protoplanetary disks, and accretion.

Our flare analysis and the derived flare properties and classifications are presented in § 2. Properties of the stars themselves are also provided. Global properties of our flares are considered in § 3 and compared to published studies of older stars.

## 2. FLARE ANALYSIS

We analyze 216 of the brightest X-ray flares from 161 of the brightest COUP young stars. This is a more than five-fold increase from the bright flare sample of Favata et al. (2005). The major steps of our analysis are presented below.

### 2.1. *Flare Sample*

Among 1616 COUP X-ray sources, 1408 have been associated with the stellar members of the Orion region (Getman et al. 2005a). With the exception of 10 hot OB-type stars, 1398 are identified as cool young members of the Orion region (Feigelson et al. 2005).

We start with the subsample consisting of the brightest 188 cool Orion stars, those with net counts NC $\geq$ 4000 as tabulated by Getman et al. (2005b, Table 4). All of them show signs of variability, i.e., their X-ray light curves are characterized by at least two Bayesian block segments (Table 7 of Getman et al.) during the 13.2 day COUP observation. The complete set of 1616 COUP light curves are available in the Source Atlas provided as a figure set in the electronic edition of Getman et al. (2005b). Individual examples of strong flares have been published in Favata et al. (2005) and Wolk et al. (2005).

Using the interactive software graphical program `function1d` in the IDL-based TARA package,[3] we identify flarelike events in which the peak count rate is $\geq$4 times that of the "characteristic" level. The characteristic level is the typical preflare or interflare, as explained by Wolk et al. (2005). We avoid the designation "quiescent" level because it probably arises from the integrated effect of many weaker flares. This results in 216 flares from 161 cool stars with median of $\sim$1500 counts. Only 20 flares have $<$600 counts.

### 2.2. *MASME Spectral Modeling*

Our analysis of flare spectral evolution is based on the method of adaptively smoothed median energy (MASME) introduced by Getman et al. (2006). We compare its results to the established method of time-resolved spectroscopy (TRS), which involves statistical fitting of multiparameter spectral models, in Appendix A. The MASME method is simpler, statistically more stable, and computationally quicker than TRS. It employs an adaptively smoothed estimator of the median energy[4] of flare counts and count rate to infer the evolution of plasma temperatures and emission measures during the flare. This procedure is similar to the analyses of Reale & Micela (1998) and Wargelin et al. (2008), which avoid nonlinear parametric flare modeling using hardness ratios.

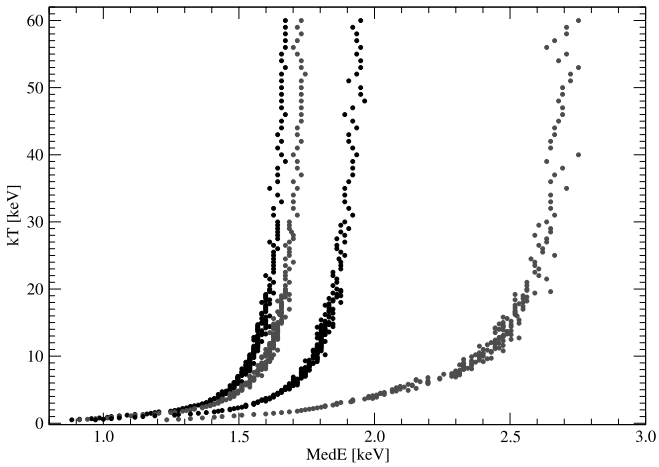


FIG. 1.—Calibration of plasma temperature vs. observed X-ray median energy for representative column densities [$\log N_{\rm H} = (20.5, 21, 21.5, 22)$ cm$^{-2}$, *left to right*] calculated from spectral simulations.

The smoothing kernel is a rectangle ("boxcar") of variable width; as it moves through the time series its width is adjusted so that it encompasses a specified number of X-ray counts. Kernels are evaluated on a time grid with bin width $\Delta t = 1.14$ ks, chosen to divide the total COUP observation span of 1140 ks into 1000 bins. Flux and median energy estimates are computed from the counts found in each of these overlapping kernels, forming smoothed flux and median energy time series which then used for spectral modeling. Similar flux and median energy time series are produced by the ACIS Extract software package.[5] For each flare, the target number of counts in the kernel is chosen such that the resulting smoothed light curve closely matches the binned light curve given in the COUP Source Atlas of Getman et al. (2005b). This generally results in $\sim$100 to $\sim$600 counts included in each kernel for the weakest to the brightest flares, respectively. The typical width of the smoothing kernel is a few kiloseconds at the peak of the flare and $\sim$10 ks at the base of the flare.

PMS X-ray spectra are typically modeled as emission by hot plasmas at one or two temperatures subject to absorption by a column density, $N_{\rm H}$. If we adopt the $N_{\rm H}$ inferred from the time-integrated spectral fits of Getman et al. (2005b) and assume that $N_{\rm H}$ does not change during the COUP observation, then we can calibrate median energies and count rates to plasma temperatures ($kT$) and emission measures (EM). Figure 1 shows the median energy to plasma temperature calibration based on simulations similar to those described by Getman et al. (2006). For each COUP source, the `fakeit` command in XSPEC (Arnaud 1996) is used to simulate a grid of high signal-to-noise ACIS-I spectra with absorbed plasma models (WABS$\times$MEKAL) and fixed column density. Simulated spectra are then passed through ACIS Extract to perform photometric analysis, including calculation of fluxes (observed count rates) and median energy. At each time point of interest, a comparison of simulated count rates with that of the observed flare provides an estimate of the flare emission measure; a comparison of simulated and observed median energies provides an estimate of the flare plasma temperature.[6]

[3] Description and code for the "Tools for ACIS Review & Analysis" (TARA) package developed at Penn State can be found at http://www.astro.psu.edu/xray/docs/TARA/.

[4] X-ray source median energy is an observed quantity (Getman et al. 2005b) and can be effectively used as an indicator of plasma temperature if the absorbing column is known, or as an indicator of column density at median energies >1.7 keV (Feigelson et al. 2005). Other researches have also found that median energies are effective spectral estimators in X-ray CCD spectroscopy (Hong et al. 2004).

[5] ACIS Extract is a *Chandra*-ACIS source extraction and analysis package developed at Penn State. It was used for the COUP data analysis and is described at http://www.astro.psu.edu/xray/docs/TARA/ae_users_guide.html.

[6] XSPEC fitting of simulated spectra using the $\chi^2$ statistic tends to overestimate plasma temperature. In order to avoid this systematic bias in our simulations, we adopt the input plasma temperature rather than the temperature derived from XSPEC fit of the simulated spectrum.

TABLE 1
FLARE PROPERTIES 1

| Source (1) | Flare No. (2) | $NC_f$ (counts) (3) | $BG_f$ (counts) (4) | $ME_f$ (keV) (5) | $t_{char1}$ (ks) (6) | $t_{char2}$ (ks) (7) | $t_{flare1}$ (ks) (8) | $t_{flare2}$ (ks) (9) | $CR_{char}$ (counts ks$^{-1}$) (10) | $CR_{flare,pk}$ (counts ks$^{-1}$) (11) | $t_{CR,pk}$ (ks) (12) | $t_{T,pk}$ (ks) (13) | $t_{EM,pk}$ (ks) (14) | $t_{exp}$ (ks) (15) | $t_{sep}$ (ks) (16) |
|---|---|---|---|---|---|---|---|---|---|---|---|---|---|---|---|
| 7..... | 1 | 3209 | 11.7 | 1.31 | 60.0 | 100.0 | 930.0 | 967.0 | 38.3 | 164.0 ± 11.5 | 951.1 | 948.9 | 951.2 | 967.0 | 960.0 |
| 9..... | 1 | 3980 | 6.1 | 1.55 | 160.0 | 200.0 | 523.0 | 558.0 | 12.8 | 210.0 ± 7.7 | 542.4 | 538.5 | 544.2 | 553.0 | 549.0 |
| 11..... | 1 | 1158 | 3.5 | 2.17 | 883.0 | 940.0 | 977.0 | 1009.0 | 3.4 | 105.5 ± 6.3 | 986.9 | 978.6 | 986.5 | 993.0 | 997.5 |
| 23..... | 1 | 4370 | 13.5 | 1.37 | 440.0 | 480.0 | 740.0 | 788.0 | 51.8 | 306.7 ± 15.5 | 747.0 | 746.0 | 747.1 | 752.0 | 750.0 |
| 27..... | 1 | 350 | 5.9 | 1.37 | 220.0 | 260.0 | 258.0 | 302.0 | 4.4 | 14.2 ± 1.8 | 282.6 | 283.2 | 285.4 | 295.0 | 295.0 |
| 27..... | 2 | 1653 | 28.1 | 1.31 | 220.0 | 260.0 | 681.0 | 890.0 | 4.4 | 19.5 ± 2.0 | 710.8 | 720.9 | 711.8 | 743.0 | 743.0 |
| 28..... | 1 | 13308 | 22.9 | 1.44 | 200.0 | 300.0 | 615.0 | 790.0 | 3.6 | 300.3 ± 10.7 | 623.6 | 616.0 | 622.9 | 680.0 | 745.0 |
| 43..... | 1 | 2744 | 7.5 | 1.42 | 470.0 | 520.0 | 665.0 | 800.0 | 4.3 | 39.4 ± 2.8 | 716.5 | 709.5 | 714.1 | 770.0 | 730.0 |
| 57..... | 1 | 724 | 0.4 | 1.26 | 910.0 | 950.0 | 185.0 | 272.0 | 3.2 | 16.7 ± 1.9 | 202.7 | 205.6 | 204.5 | 221.0 | 233.5 |
| 57..... | 2 | 306 | 0.2 | 1.22 | 910.0 | 950.0 | 852.0 | 900.0 | 3.2 | 11.2 ± 1.6 | 870.6 | 864.6 | 871.4 | 879.0 | 883.0 |
| 62..... | 1 | 5933 | 30.6 | 1.39 | 245.0 | 295.0 | 260.0 | 788.0 | 3.0 | 30.9 ± 2.5 | 505.2 | 465.6 | 535.1 | 560.0 | 650.0 |
| 62..... | 2 | 885 | 5.7 | 1.42 | 245.0 | 295.0 | 902.0 | 1000.0 | 3.0 | 19.3 ± 2.0 | 939.1 | 938.7 | 946.6 | 963.0 | 953.0 |
| 66..... | 1 | 1667 | 4.7 | 1.52 | 0.0 | 100.0 | 468.0 | 658.0 | 1.6 | 25.7 ± 2.3 | 539.5 | 502.0 | 515.7 | 558.0 | 560.0 |
| 67..... | 1 | 638 | 1.8 | 1.29 | 212.0 | 250.0 | 923.0 | 972.0 | 6.5 | 28.1 ± 2.5 | 933.7 | 931.8 | 934.1 | 948.0 | 948.0 |
| 71..... | 1 | 2654 | 10.9 | 1.15 | 980.0 | 1010.0 | 481.0 | 770.0 | 3.6 | 35.1 ± 2.7 | 505.2 | 504.3 | 507.7 | 518.0 | 561.0 |

NOTES.—Col. (1): COUP source number from Getman et al. (2005b). Col. (2): Flare number. Cols. (3)–(5): Estimated net flare counts, background counts during the flare, and median X-ray energy of flare counts. Cols. (6)–(7): Start and stop times for measurement of the "characteristic" state. All times are measured from the start time of the COUP observation. Cols. (8)–(9): Observed start and stop times of the flare. Col. (10): Median count rate of the "characteristic" state. Col. (11): Observed flare peak count rate. Cols. (12)–(14): Time points when flare count rate, plasma temperature, and emission measure have maximum values. Col. (15): Time point until which the light curve exhibits a pure exponential decay. Col. (16): Separation time point between two distinct decay phases. This is relevant for cases with double slope decays (see $Flag_1$ from Table 2). Table 1 is published in its entirety in the electronic edition of the *Astrophysical Journal*. A portion is shown here for guidance regarding its form and content.

Due to the curved dependency of the true plasma temperature on observed median energy (Fig. 1), estimated plasma temperatures of $\lesssim$200 MK ($\lesssim$17 keV) are expected to be quite reliable, while temperature values of $\gtrsim$200 MK are much more uncertain. The accuracy of our temperature estimates is discussed in detail in Appendix B. We find that the 1 $\sigma$ errors of peak flare temperature are generally $<$30% for $T_{obs,pk} < 50$ MK, around 45% for $T_{obs,pk} \sim 200$ MK, but reach up to 65% for the hottest flares. Nonetheless, we establish that superhot flares, with derived peak temperatures above 200 MK, are definitely hotter than 100 MK.

The major advantage of the MASME over TRS is that spectral analysis is performed at dozens of points along the decay phase of a flare light curve, rather than at just a handful of points typical of TRS. This higher time resolution often results in the discovery of a more detailed, often more complex flare behavior. One drawback of the MASME procedure is that the weak "characteristic" background is ignored. We discuss these issues further in Appendix A, where the TRS and MASME analysis methods are carefully compared.

### 2.3. *Loop Modeling*

One of the major goals of our flare analysis is to derive sizes of coronal structures responsible for the COUP flares. We employ the time-dependent hydrodynamic model of Reale et al. (1997) for a single coronal magnetic loop. Reale et al. establish a formula for estimating loop size, taking into account the possibility of prolonged heating during the decay phase. They find

$$L = \frac{\tau_d \sqrt{T_{pk}}}{3.7 \times 10^{-4} F(\zeta)}, \quad (1)$$

where $L$ is the half-length of the loop (cm), $\tau_d$ is the flare decay $e$-folding timescale (s), and $T_{pk}$ is the flare maximum temperature at the loop apex (K). The term $F(\zeta)$ is a correction factor for prolonged heating that is a function of the slope $\zeta$ of the trajectory in the temperature-density diagram. In practice, $F(\zeta)$ and $T_{pk}$ must be calibrated for each X-ray telescope and detector; the slope $\zeta$ is usually measured in the log $T$– log (EM$^{1/2}$) plane, where EM is the changing emission measure and EM$^{1/2}$ is used as a proxy for the plasma density. We reproduce calibration formulas for $F(\zeta)$ and $T_{pk}$ derived for *Chandra*-ACIS in Favata et al. (2005),

$$F(\zeta) = \frac{0.63}{\zeta - 0.32} + 1.41, \quad (2)$$

$$T_{pk} = 0.068 T_{obs}^{1.2}, \quad (3)$$

where $T_{pk}$ is a temperature at the loop apex (K), and $T_{obs}$ is an "average" loop temperature (K) obtained from our *Chandra*-ACIS data.

This model is simplistic in a number of ways. It assumes the plasma has a uniform density with unity filling factor, confined within a single semicircular loop of uniform cross section and 10 : 1 length : radius shape. Furthermore, the model assumes that this geometry remains unaltered during the flare, that energy is efficiently transported along magnetic field lines of the loop, and that there is continuous energy balance between the loop heating and the thermal conduction and radiative losses. Despite these limitations, the Reale et al. (1997) model has been applied successfully to a variety of solar and stellar flares (e.g., Crespo-Chacón et al. 2007; Testa et al. 2007; Franciosini et al. 2007; Giardino et al. 2007), including the COUP flares studied by Favata et al. (2005). It has advantages over earlier and simpler cooling loop models (e.g., Rosner et al. 1978; Serio et al. 1991) which neglect reheating during the decay phase and thereby tend to overestimate loop sizes.

### 2.4. *Flare Characteristics*

Empirical and derived quantities obtained in our MASME flare analysis are reported in Tables 1 and 2. We explain them in this section and illustrate them in detail for one flare in the print

TABLE 2
FLARE PROPERTIES 2

| Source (1) | FlareNo. (2) | $\tau_r$ (ks) (3) | $\tau_{d1}$ (ks) (4) | $\tau_{d2}$ (ks) (5) | $\log L_{\rm X,pk}$ (erg s$^{-1}$) (6) | $T_{\rm obs,pk}$ (MK) (7) | $\rm EM_{pk}$ ($10^{53}$ cm$^{-3}$) (8) | $T_{\rm EM,pk}$ (MK) (9) | $\zeta_1$ (10) | $\zeta_2$ (11) | $\zeta_3$ (12) | $L_1$ ($10^{10}$ cm) (13) | $L_2$ ($10^{10}$ cm) (14) | $L_{\rm lim}$ ($10^{10}$ cm) (15) | $\rm Flag_1$ (16) | Type (17) |
|---|---|---|---|---|---|---|---|---|---|---|---|---|---|---|---|---|
| 7..... | 1 | 13.5 | 13.0 | 13.0 | 31.62 | 40.62 | 40.37 | 27.85 | 0.6 | 1.3 | −1.1 | 12.97 | 12.97 | 26.89 | 02 | typ |
| 9..... | 1 | 10.0 | 19.2 | 19.5 | 32.18 | 103.28 | 117.11 | 32.49 | −0.1 | −0.6 | 0.4 | | ... | 44.06 | 44 | inc |
| 11..... | 1 | 3.4 | 6.5 | 8.7 | 31.84 | 696.29 | 47.67 | 696.29 | 2.7 | 0.0 | 6.2 | 55.03 | 74.06 | 124.41 | 01 | stp |
| 23..... | 1 | 2.4 | 5.5 | 14.9 | 31.98 | 60.34 | 72.48 | 54.54 | 1.2 | 8.4 | 0.6 | 4.15 | 21.22 | 45.93 | 13 | typ |
| 27..... | 1 | 15.4 | 27.9 | 22.0 | 30.57 | 40.62 | 3.32 | 31.33 | 2.3 | 2.5 | 0.5 | 28.24 | 35.81 | 61.87 | 01 | inc |
| 27..... | 2 | 21.0 | 70.6 | 123.3 | 30.69 | 33.65 | 4.87 | 26.69 | 0.6 | −0.0 | 0.6 | 42.79 | 74.71 | 248.25 | 01 | stp |
| 28..... | 1 | 208.4 | 30.9 | 40.8 | 32.05 | 67.31 | 86.29 | 41.78 | 0.5 | 0.7 | −2.9 | 25.03 | 33.07 | 107.57 | 02 | inc |
| 43..... | 1 | 50.6 | 55.5 | 55.0 | 31.18 | 59.18 | 11.96 | 41.78 | 1.4 | 4.2 | 0.8 | 50.72 | 51.20 | 146.19 | 03 | srf |
| 57..... | 1 | 7.4 | 31.7 | 52.2 | 31.10 | 52.22 | 10.51 | 33.65 | 1.3 | 2.8 | 1.6 | 35.78 | 58.98 | 120.77 | 01 | dbl |
| 57..... | 2 | 17.8 | ... | 22.5 | 30.91 | 27.85 | 8.42 | 22.05 | 0.3 | 0.5 | 0.8 | 0.39 | 0.39 | 40.39 | 01 | oth |
| 62..... | 1 | 117.0 | 232.0 | 197.6 | 30.94 | 62.67 | 7.83 | 23.21 | 0.3 | 0.4 | −0.5 | ... | ... | 429.47 | 44 | oth |
| 62..... | 2 | 18.4 | 39.0 | 41.6 | 30.77 | 94.00 | 3.92 | 48.74 | 2.0 | 10.3 | 1.9 | 62.54 | 66.79 | 120.30 | 03 | typ |
| 66..... | 1 | 52.2 | 49.8 | 76.9 | 31.03 | 568.64 | 8.13 | 568.64 | 2.8 | 2.1 | 1.6 | 332.26 | 512.68 | 970.41 | 03 | dbl |
| 67..... | 1 | 5.4 | 14.7 | 23.4 | 31.00 | 47.58 | 8.77 | 34.81 | 1.0 | 1.8 | 0.0 | 14.63 | 30.11 | 55.14 | 12 | typ |
| 71..... | 1 | 12.2 | 11.5 | 107.6 | 30.94 | 35.97 | 7.91 | 35.97 | 1.0 | 1.9 | 0.5 | 5.71 | 108.37 | 259.18 | 13 | stp |

NOTES.—Col. (1): COUP source number from Getman et al. (2005b). Col. (2): Flare number. Col. (3): Rise *e*-folding timescale. Cols. (4)–(5): Decay *e*-folding timescales: $\tau_{d1}$ is measured within the time interval $[t_{\rm CR,pk}–t_{\rm exp}]$, and $\tau_{d2}$ is measured within the time interval $[t_{\rm CR,pk}–t_{\rm flare2}]$ (see notes to Table 1 for the description of $t_{\rm flare2}$, $t_{\rm CR,pk}$, and $t_{\rm exp}$). Col. (6): Flare peak X-ray luminosity. Col. (7): Flare peak observed plasma temperature. Col. (8): Flare peak emission measure. Col. (9): Observed plasma temperature at the time point when the emission measure has maximum value $\rm EM_{pk}$. Cols. (10)–(12): Inferred slopes of the trajectory in the $\log T$– $\log (\rm EM)^{1/2}$ diagram: $\zeta_1$ is the average slope derived over the full $[t_{\rm EM,pk}–t_{\rm flare2}]$ decay time interval, $\zeta_2$ is the slope derived within the $[t_{\rm EM,pk}–t_{\rm sep}]$ interval, and $\zeta_2$ is the slope derived within the $[t_{\rm sep}–t_{\rm flare2}]$ interval (see totes to Table 1 for the description of $t_{\rm flare2}$, $t_{\rm EM,pk}$, and $t_{\rm sep}$). Cols. (13)–(14): Inferred length range of the flaring structure $[L_1–L_2]$ obtained under the assumption of sustained heating using the combination of both decay timescales, $\tau_{d1}$ and $\tau_{d2}$, and inferred slopes defined by $\rm Flag_1$. Col. (15): The limiting maximum loop length assuming the scaling law of Serio et al. (1991) for a freely decaying loop with no sustained heating. Col. (16): $\rm Flag_1$ defines the best or dominant (over most of the decay time) slope or a combination of possible slopes (generally for a double slope decay), which, in combination with decay timescales $\tau_{d1}$ and $\tau_{d2}$, are used to estimate the range of flaring loop sizes: 01 = $\zeta_1$; 02 = $\zeta_2$; 03 = $\zeta_3$; 12 = $\zeta_1, \zeta_2$; 13 = $\zeta_1, \zeta_3$; 23 = $\zeta_2, \zeta_3$; and 44 = unable to estimate loop sizes. Col. (17): Flare morphological classification: typ = typical, stp = flare with step decay, srf = slow rise and/or top flat, dbl = double flare, inc = incomplete, oth = other. Table 2 is published in its entirety in the electronic edition of the *Astrophysical Journal* . A portion is shown here for guidance regarding its form and content.

sample of Figure Set 2; the electronic edition of this paper contains our full sample (216 flares). Many sources show more than one bright flare during the 13 day COUP observation. In two sources (COUP 682 and 1463) we have analyzed four bright flares, 10 sources have three flares; and 43 sources have two flares. The "Flare No." quantity in conjunction with the source number in Tables 1 and 2 provides a unique identifier for each of the 216 flares.

Several reported quantities are associated with the characteristic level between flares. The quantities $t_{\rm char1}$ and $t_{\rm char2}$ represent the start and stop times (offsets from the beginning of the COUP observation) of the "characteristic" light curve block with the lowest count rate. These intervals were defined visually using the interactive graphical tool `function1d` in the TARA package; the duration of this block is always >20 ks. The median count rate in this interval is $\rm CR_{char}$. These quantities are labeled in blue in Figure 2*a*.

The flare events are defined by the quantities $t_{\rm flare1}$ and $t_{\rm flare2}$ (labeled in red in Figs. 2*a* and 2*b*) giving start and stop times for the flare, with the peak count rate given by $\rm CR_{flare,pk}$. Both $\rm CR_{char}$ and $\rm CR_{flare,pk}$ are obtained from the binned histogram data (black points in Fig. 2*a* and 2*b*), and not from the adaptively smoothed version of the light curve (dashed blue curve in Fig. 2*b*). Following the recommendation of Reale et al. (1997), we choose the flare stop time as the moment at which the flare count rate has decreased to ~1/10 of the peak value. However, often an earlier $t_{\rm flare2}$ was chosen because a COUP observational gap or minor flare fell near the end of the studied flare.

The quantity $\rm BG_{\it f}$ represents the number of background counts expected in the flare time interval, obtained by scaling the source's background from Getman et al. (2005b) to the duration of the flare. With a few exceptions, this correction is very small ($\rm BG_{\it f}/NC_{\it f}$ <0.02). We therefore have chosen to ignore the background in estimating the median energy, $\rm ME_{\it f}$, during the flare.

The quantities $\tau_r$, $\tau_{d1}$, and $\tau_{d2}$ give 1/*e* rise and decay times determined from a least-squares fit of the count rate histogram. This is illustrated by the red and green curves in Figure 2*b*. These are fits of the exponential function $\rm CR = CR_{flare,pk} \times \exp[(\it t - t_{CR,pk})/\tau]$, where $t_{\rm CR,pk}$ is the time of the peak count rate, and $\tau$ is $-\tau_{d1,2}$ or $+\tau_r$. Decays of many COUP flares deviate from a pure exponential shape. This is not unusual; Osten & Brown (1999) found that 8 of 33 flares from RS CVn binaries observed with the *Extreme Ultraviolet Explorer* showed changing exponential decays. Complex, often bumpy, decays arise from both reheating of a single loop and the illumination of associated loops. These issues are discussed in the next section. For COUP X-ray flares, we introduce two decay *e*-folding timescales, $\tau_{d1}$ for the initial purely exponential decay phase lasting at least to the time point $t_{\rm exp}$, and $\tau_{d2}$ for the *e*-folding decay timescale averaged over the entire decay phase from $t_{\rm CR,pk}$ until $t_{\rm flare2}$. As the data become less consistent with a single exponential decay model, the difference between $\tau_{d1}$ and $\tau_{d2}$ increases.

The adaptively smoothed count rate and median energy time series are shown as the blue dashed curve in Figure 2*b* and the black symbols in Figure 2*c*. These are converted into plasma temperature (Fig. 2*d*) and flare emission measure (Fig. 2*e*) time series using calibration simulations described in § 2.2. Information on maximum values of flare X-ray luminosity ($\log L_{\rm X,pk}$), observed temperature ($T_{\rm obs,pk}$), emission measure ($\rm EM_{pk}$), and corresponding time points, such as $t_{T,\rm pk}$ and $t_{\rm EM,pk}$ is then easily obtained.

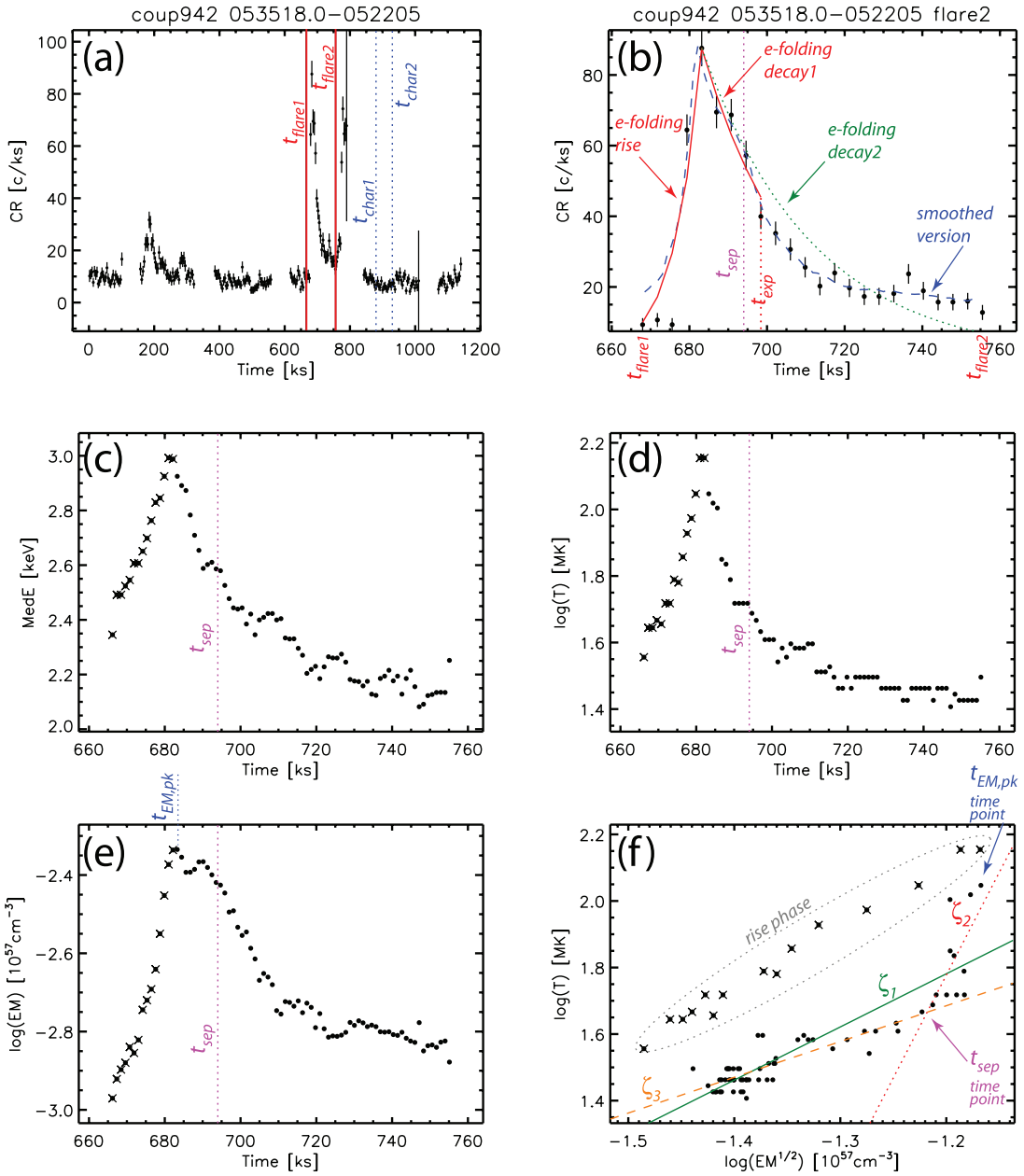


FIG. SET 2.—Illustration of our X-ray spectral modeling procedure using flare 2 of COUP 942, using the method of adaptively smoothed median energy (MASME). Details on specific symbols and lines are provided in § 2.4. (*a*) X-ray light curve over the whole COUP observation (six nearly consecutive exposures) from the COUP Atlas of Getman et al. (2005b). (*b*) Light curve of the flare in binned histogram (*black*) and adaptively smoothed (*blue*) representations. (*c*) Evolution of the median energy. (*d*) Evolution of the plasma temperature. (*e*) Evolution of the emission measure. (*f*) Evolution in the $\log T - \log\sqrt{(\mathrm{EM})}$ plane [*See the electronic edition of the Journal for the full COUP flare atlas, Figs. 2.1–2.216.*]

Considering that the proper decay phase begins at the time of the density peak, not at the count rate or temperature peak (at least for an impulsive flare event), Reale (2007) encourages using the temperature at the density peak rather than the brightness peak when determine the loop length. We thus introduce the quantity $T_{\mathrm{EM,pk}}$, the plasma temperature at the peak of the emission measure. Crosses in Figure 2*c*-2*f* mark the rise phase, the time period prior to the moment when the emission measure reaches its maximum value, while circles mark the decay phase of the flare.

Several remaining obtained quantities listed in Tables 1 and 2 and shown in Figure Set 2 remain to be discussed. The quantity $t_{\mathrm{sep}}$ is the time point separating the two distinct decay phases when a simple exponential decay is not present. The quantities $\zeta_1$, $\zeta_2$, and $\zeta_3$ are the inferred slopes of the trajectory in the $\log T - \log(\mathrm{EM}^{1/2})$ diagram. The morphological flare type is discussed in § 2.5. The quantities $L_1$, $L_2$, and $L_{\mathrm{lim}}$ are the lengths of the flaring structures inferred from equation (1). $\mathrm{Flag}_1$ provides details on a number of decay phases and indicates the "dominant" slope used in estimation of loop sizes.

### 2.5. *Flare Morphology and Classification*

In order to obtain optimal results within the framework of the Reale et al. (1997) single-loop model, the X-ray light curve should not present significant deviations from a pure exponential decay, and the decay trajectory in the $\log T - \log(\mathrm{EM}^{1/2})$ plane should be linear. Strong deviations from an exponential decay and the absence of a single linear trajectory are indications of more complex events, such as multiple coronal loops (e.g., sequential reconnection

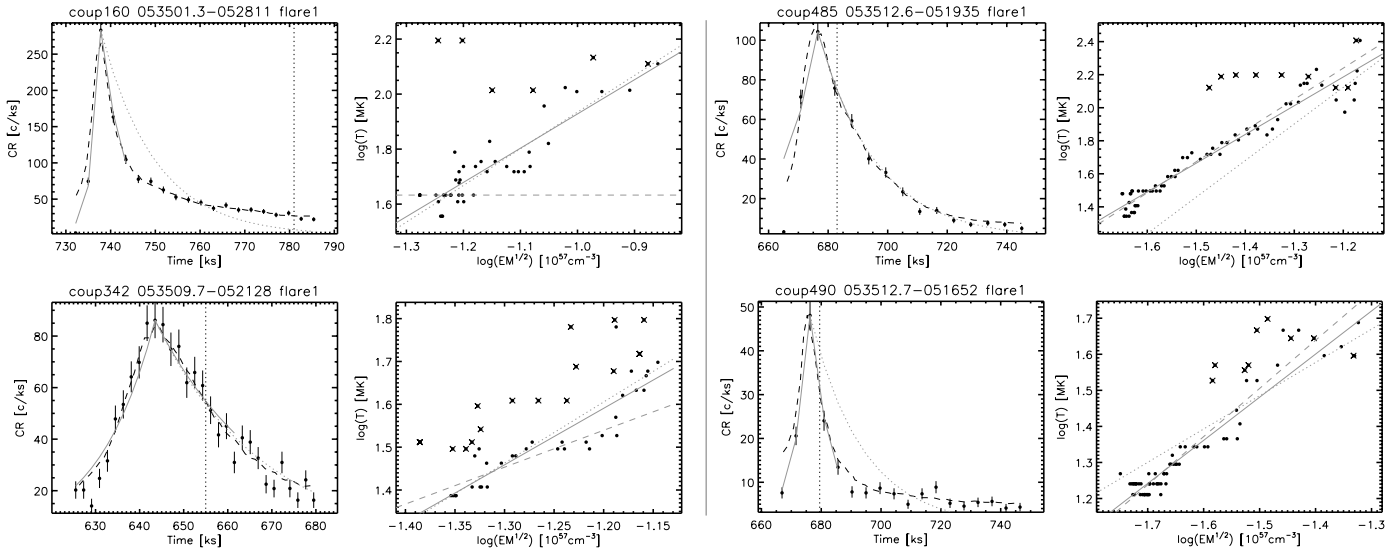


FIG. 3.—Light curves and inferred temperature-density trajectories for four representative flares in the class "typical."

in a loop arcade as in a two-ribbon solar flare) and/or complex heating sequences within a single loop (e.g., Reale et al. 2004; Reale 2007).

However, even in the case of complex flares it is appropriate to apply the single-loop approach to a light curve segment if there is an indication for the presence of a single dominant loop. Reale (2007) argues that when multiple loop structures are involved in the flare, the rise and early decay are often dominated by a single primary loop. This is supported by detailed time-dependent loop modeling of the "bumpy" decay flare observed with *XMM-Newton* on Proxima Centauri (Reale et al. 2004). Here it was found that the X-ray emission from the primary single loop dominated the initial phases of the flare, but later was overlapped by the emission from an arcade of several loops of similar size as the primary loop.

Similar complex, multiple-component flares have been seen in the contemporary Sun, including the well-studied Bastille Day flare in 2000 July (Aschwanden & Alexander 2001) and a variety of bumpy flares seen with the *GOES* and *TRACE* satellites. They are seen in both two-ribbon flares and compact flares.[7] Reale et al. (2004) speculate that this is a common pattern in large solar and stellar magnetic reconnection.

We have adapted these ideas, together with our careful examination of the X-ray morphology of the 216 COUP flares, into a classification scheme consisting of four well-defined groups and two groups containing flares that cannot be clearly characterized. In order of their morphological complexity, these classes are:

*Typical flares* (typ).—These have simple X-ray light curves with rapid monotonic rise and generally slower monotonic decay. This is the most populous class, making up 84 of the 216 COUP

[7] Examples of "bumpy" solar flares seen in soft X-rays by *GOES 8*, and EUV light by *TRACE*, can be found in the *TRACE* Flare Catalog (http://hea-www.harvard.edu/trace/flare_catalog/index.html). See, for example, the 2005 January 16 (22:03:00 UT, M2.4) and September 8 (20:29:00 UT, M2.1) two-ribbon flares, and the 2005 November 14 (22:00:00 UT, M1.0) and December 2 (10:12:00 UT, M7.8) compact flares.

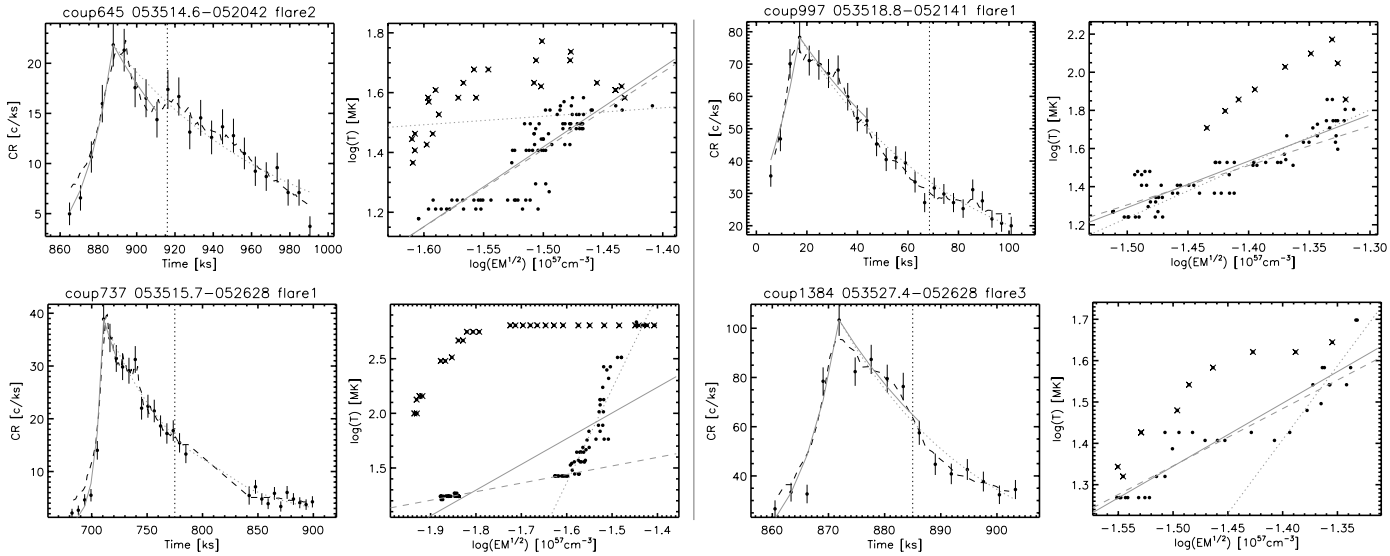


FIG. 4.—Light curves and inferred temperature-density trajectories for four representative flares in the class "step."

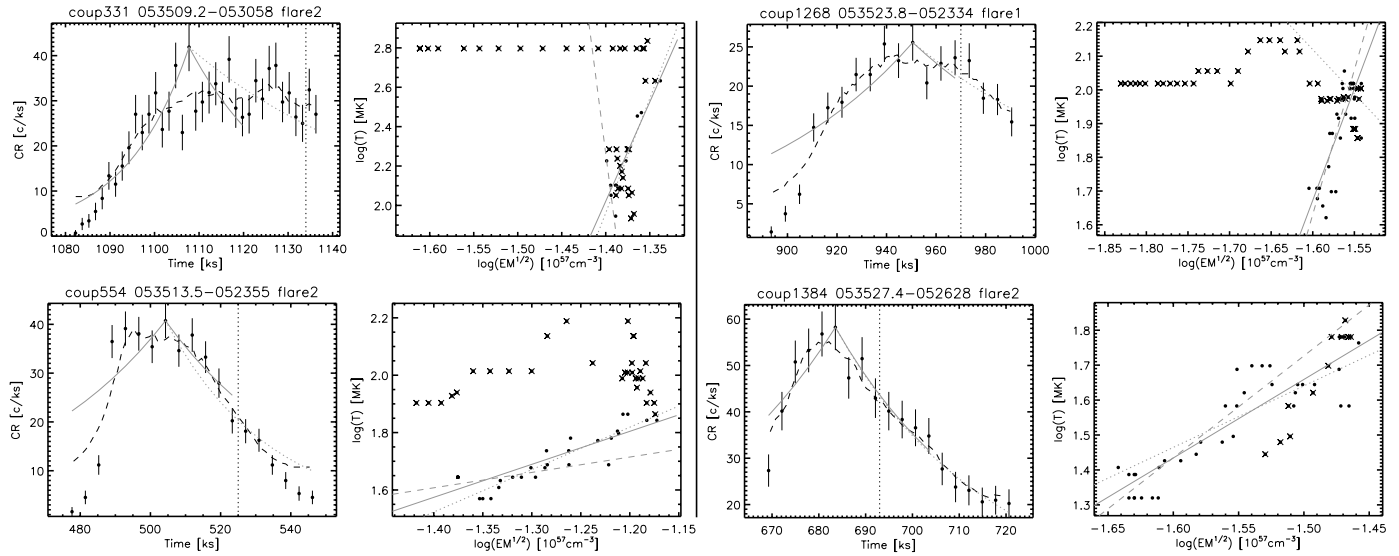


FIG. 5.—Light curves and inferred temperature-density trajectories for four representative flares in the class "slow rise and/or top flat."

flares. Seven of them have symmetrical light curve shape with similar rise and decay timescales.

*Step flares* (stp).—These look like a typical flare, but with a shoulder or bump overlaid on its decay phase. These morphologies are commonly seen on the Sun and are due to either a reheating event or a triggered reconnection in a nearby magnetic loop. A total of 38 COUP flares fall into this category. The "bumpy" decay flare from Proxima Centauri (Reale et al. 2004) is a good example of this class.

*Double flares* (dbl).—Double flares look like two overlapped typical flares, or a typical flare with a bump on its rise phase. Eight flares clearly show double peaks in appearance.

*Slow rise, top flat flares* (srtf=srf).—These are more complex events, where variations appear to occur more slowly than in most flares. They have slow rises, long duration peaks, and/or very long decays. One of these (a T Tauri star in the Orion B cloud) was discussed by Grosso et al. (2004) without a clear interpretation, and a few (COUP 43, 597, 1384) appear in Favata et al. (2005; see their Fig. 9). In our study, 20 COUP flares are in this class.

*Incomplete* (inc).—This group consists of the 42 flares whose *Chandra* light curves are severely interrupted by COUP observational gaps.

*Others* (oth).—These are 24 flares with poorly defined shapes generally due to their low statistics.

The four well-defined classes are illustrated in Figures 3–6, along with their inferred trajectories on the log $T$– log (EM$^{1/2}$) plane. For about 56% (34%) out of 84 (38) typical (step) flares, trajectories can be approximated by a single slope. In these cases, the derived loop sizes are most reliable. In many of the remaining cases, two slopes can be discerned in the log $T$– log (EM$^{1/2}$) trajectories, while in some the patterns are too complex to interpret. Flare classifications based on light curve morphology may not be correct in all cases; for example, a few flares with simple light curve decays classified as typical flares show double-peaked temperature evolutions. These effects are included in the loop reheating model (§ 2.3) and thus in the derived loop sizes, but such flares have not been reclassified as double-peaked flares.

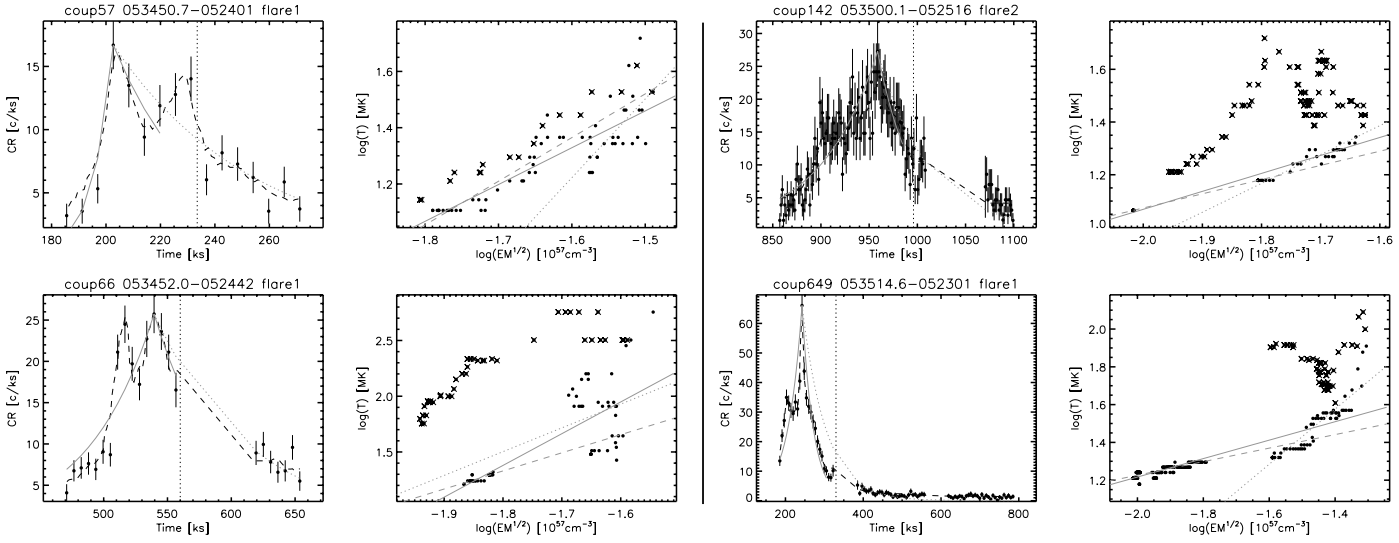


FIG. 6.—Light curves and inferred temperature-density trajectories for four representative flares in the class "double."

$Flag_1$ in Table 2 encodes the number of inferred dominant decay slopes of log $T$– log (EM$^{1/2}$) trajectories; values of 01 ($=\zeta_1$), 02 ($=\zeta_2$), and 03 ($=\zeta_3$) refer to a single dominant slope, while 12 ($=\zeta_1,\zeta_2$), 13 ($=\zeta_1,\zeta_3$), and 23 ($=\zeta_2,\zeta_3$) refer to a double slope. In cases with a single slope, the slope value used is generally the average slope $\zeta_1$ (green solid line in Fig. 2*f*) derived within the whole flare time interval. In double-slope cases, the two slopes are generally described by $\zeta_2$ (slope within the initial decay; red dotted line in Fig. 2*f*) and $\zeta_3$ (slope within the late decay; orange dashed line in Fig. 2*f*) separated in time by the point $t_{\rm sep}$ (given in Table 1).

While we do not know of a similar flare classification effort in other solar or stellar studies, a similar range of flare behaviors is seen in the contemporary Sun. Analysis of *Solar Maximum Mission* observations of 66 solar flares by Sylwester et al. (1993) showed that 26% of flares have log $T$– log (EM$^{1/2}$) trajectories with two or more branches, while the majority show single-branched trajectories.

### 2.6. *Flare Loop Sizes*

Due to the complexity of flare behavior in our sample (described above, shown in Fig. Set 2), it seems reasonable to present a range of possible loop sizes rather than a single size value for a given flare. The range of sizes is derived assuming the presence of dominant coronal structures even during the complex flare events. This approach should be suitable for the goals of the current work, which examines statistical relationships between flare behaviors, magnetic loop sizes, global star properties, protoplanetary disks, and accretion.

The loop size range ($[L_1 : L_2]$, reported in Table 2) is estimated through equations (1)−(3) in § 2.3 using the combination of both decay timescales (initial, $\tau_{d1}$, and averaged over the entire decay phase, $\tau_{d2}$) with the decay slopes indicated by $Flag_1$. If a single dominant slope is indicated by $Flag_1$, then two loop size estimates emerge after applying both decay timescales with the combination of that single slope. If a double slope is indicated by $Flag_1$, then two loop size estimates emerge in the following ways: for $Flag_1 = 23$, we combine $\tau_{d1}$ with $\zeta_2$ and $\tau_{d2}$ with $\zeta_3$; for $Flag_1 = 13$, we combine $\tau_{d1}$ with $\zeta_1$ and $\tau_{d2}$ with $\zeta_3$; and for $Flag_1 = 12$, we combine $\tau_{d1}$ with $\zeta_2$ and $\tau_{d2}$ with $\zeta_1$. In equation (3), $T_{\rm obs}$ is the observed *Chandra*-ACIS flare temperature at the peak of the emission measure ($T_{\rm EM,pk}$ from Table 2).

$L_{\rm lim}$, the limiting maximum loop length assuming a freely decaying loop with no sustained heating, is computed using $\tau_{d2}$ in equation (14) of Serio et al. (1991). This estimate is based on the older cooling loop theory of Rosner et al. (1978) and may overestimate loop lengths if reheating or triggered events extend the decay phase.

We compared our methodology with the well-studied case of the 2001 August flare on the dMe star Proxima Centauri observed with *XMM-Newton* (Reale et al. 2004). This flare has a "bumpy" decay similar to our "step" (stp) flares. Using our procedures, we obtain $\zeta_1 = 0.6$, $\zeta_2 = 0.7$, $\zeta_3 = 0.4$, $\tau_{d1} = 1.7$ ks, $\tau_{d2} = 3.3$ ks, $t_{\rm sep} = 4.7$ ks, and $Flag_1 = 01$. The inferred loop size range is $L_1 = 5\times10^9$ cm and $L_2 = 1\times10^{10}$ cm. Reale et al. (2004) obtained a value of $1\times10^{10}$ from a detailed time-dependent hydrodynamic model of the flare evolution. We conclude that our procedures are consistent with other analyses of similar complicated flares.

### 2.7. *Collected Source Properties*

Properties of the 161 COUP stars hosting our flare sample are presented in Table 3. These stellar properties will be extensively used in Paper II. Many of the quantities have been taken from the COUP tables of Getman et al. (2005b), including time-integrated net counts, background counts, median energy, and column density. The $JHK_s$ magnitudes were obtained from the merged 2MASS-VLT catalog, with a flag indicating quality of the 2MASS photometry. Optical data include the 8542 Å Ca II line strength as an accretion indicator, and stellar mass and radius estimated from position in the Hertzsprung-Russell diagram. See Getman et al. (2005b) for full details and references for these quantities. Stellar rotational periods are taken from the extended rotational data collection of Flaccomio et al. (2005). For stars with known masses ($M$) and rotational periods ($P$), we calculate the Keplerian corotation radius where centrifugal force balances gravity from $R_{\rm cor} = (GMP^2/4\pi^2)^{1/3}$.

The near-infrared (NIR) color excess $\Delta(H-K_s)$, an indicator of dusty inner circumstellar disks, is calculated here as an excess from the rightmost reddening vector on the $J-H$ vs. $H-K_s$ color-color diagram originating at $\sim$0.1 $M_\odot$, assuming an age of 1 Myr and using PMS models of Siess et al. (2000). The value for $\Delta(H-K_s)$ is given only for sources with reliable 2MASS photometry (Flag = AAA000).

A more sensitive measure of disk dust is derived from mid-infrared (MIR) images of the Orion region in the 3.6 and 4.5 $\mu$m IRAC bands using the *Spitzer* archived data (*Spitzer* observing program 50; PI: G. Fazio). For each band, the $3\times4$ shallow maps, each with 24 dither pointings, processed by the *Spitzer* Science Center pipeline (ver. S14.0.0) were combined into one mosaic with pixel size 0.86″ using IDL software developed by R. Gutermuth of the IRAC instrumental team. Aperture photometry was performed with the routine `aper.pro` in the IDLPHOT package[8] for isolated COUP sources using an aperture radius of 4 pixels, with a 4−8 pixel annulus for sky subtraction. For these aperture and sky regions, we adopted zero-point magnitude values of 19.490 and 18.751 mag for the 3.6 and 4.5 $\mu$m bands, respectively (K. Luhman 2007, private communication). High signal-to-noise ratio photometric results in both bands are presented for 112 stars in Table 3. The majority of stars without MIR photometry are those located in the outer regions of the Orion Nebula, where [3.6] and [4.5] images do not overlap. For several sources located near the BN/KL region, MIR photometry is unreliable due to strong nebular contamination in infrared images, and is omitted.

## 3. RESULTS

### 3.1. *Global Flare Properties*

Figure 7 summarizes some of the inferred physical properties of the COUP flares in the form of univariate cumulative distributions differentiated by the flare morphological classes defined in § 2.5. The panels plot distributions of several quantities relating to flare rise and decay timescales, peak luminosities, and peak temperatures.

Figure 7*a* shows that 90% of these powerful COUP flares have rise times between 1 hr and 1 day (3–100 ks). Typical (typ) and step (stp) flares have similar rise times, with medians around $\sim$3 hr (10 ks). In contrast, as expected from their class definition, slow-rise top-flat (srtf) flares have much longer rise timescales, with median around 12 hr (44 ks).[9] It is unclear whether this slow

[8] IDLPHOT is available at http://www.idlastro.gsfc.nasa.gov/ftp/pro/idlphot/aaareadme.txt.

[9] We caution that our procedure for estimating the *e*-folding rise timescales for COUP "srtf" flares, in which the rise phase is defined as the time interval between the flare start and the time point with a maximum observed count rate, may give longer timescales than those derived in other works. For example, Grosso et al. (2004) report $\tau_{\rm rise} \sim 2$ hr (7.2 ks) for the slow-rise flare in LkH$\alpha$ 312 by restricting the rise to the period of very rapid count rate change. For this flare, our procedure would give $\tau_{\rm rise} \sim 5$ hr ($\sim$20 ks).

TABLE 3
COUP Star Properties

| Source (1) | NC (counts) (2) | BG (counts) (3) | ME (keV) (4) | $\log N_{\rm H}$ ($\rm cm^{-2}$) (5) | $J$ (mag) (6) | $H$ (mag) (7) | $K_s$ (mag) (8) | Flag (9) | $\Delta(H-K_s)$ (mag) (10) | [3.6] (mag) (11) | [4.5] (mag) (12) | $M$ ($M_\odot$) (13) | $R$ ($10^{10}$ cm) (14) | $P$ (day) (15) | $R_{\rm cor}$ ($10^{10}$ cm) (16) | EW(Ca II) (Å) (17) |
|---|---|---|---|---|---|---|---|---|---|---|---|---|---|---|---|---|
| 7..... | 41952 | 362 | 1.20 | 20.93 | 8.85 | 8.10 | 7.95 | AAA000 | −0.28 | ... | ... | 2.12 | 43.61 | ... | ... | ... |
| 9..... | 16271 | 199 | 1.34 | 21.37 | 10.22 | 9.65 | 9.46 | AAA000 | −0.15 | ... | ... | 2.11 | 20.72 | ... | ... | ... |
| 11..... | 5700 | 123 | 1.53 | 21.69 | 10.53 | 9.46 | 8.60 | AAA000 | 0.25 | ... | ... | 0.69 | 24.22 | ... | ... | −14.60 |
| 23..... | 55449 | 320 | 1.29 | 21.24 | 10.01 | 9.33 | 9.09 | AAA000 | −0.16 | 8.873 ± 0.003 | 8.817 ± 0.002 | 2.17 | 26.74 | 3.45 | 86.69 | ... |
| 27..... | 5948 | 153 | 1.26 | 21.08 | 12.16 | 11.37 | 11.05 | AAA000 | −0.14 | 10.855 ± 0.005 | 10.789 ± 0.004 | 0.53 | 12.67 | 1.50 | 31.10 | 1.80 |
| 28..... | 20863 | 149 | 1.39 | 21.10 | 11.53 | 10.84 | 10.53 | AAA000 | −0.09 | 10.332 ± 0.004 | 10.264 ± 0.004 | 0.53 | 16.10 | 4.41 | 63.83 | 1.60 |
| 43..... | 7021 | 63 | 1.32 | 21.27 | 11.23 | 10.38 | 10.08 | AAA000 | −0.19 | 9.781 ± 0.005 | 9.716 ± 0.005 | 0.40 | 20.44 | ... | ... | 1.40 |
| 57..... | 4093 | 5 | 1.13 | 20.68 | 11.01 | 10.53 | 10.28 | AEE000 | ... | 10.016 ± 0.003 | 9.988 ± 0.004 | 1.19 | 15.19 | 2.34 | 54.78 | 1.60 |
| 62..... | 9294 | 66 | 1.39 | 21.08 | 11.23 | 10.21 | 9.53 | AAA000 | 0.10 | 8.530 ± 0.003 | 8.049 ± 0.002 | 1.52 | 13.16 | 6.63 | 119.00 | 0.00 |
| 66..... | 6237 | 28 | 1.37 | 21.04 | 12.13 | 11.20 | 10.63 | AAA000 | 0.04 | 9.713 ± 0.003 | 9.249 ± 0.002 | 0.24 | 12.74 | ... | ... | −2.80 |
| 67..... | 7690 | 41 | 1.23 | 21.24 | 10.85 | 9.97 | 9.62 | AAA000 | −0.16 | 9.177 ± 0.011 | 8.878 ± 0.007 | 0.29 | 27.30 | 8.83 | 82.93 | 0.00 |
| 71..... | 6597 | 43 | 1.10 | 20.00 | 11.88 | 11.19 | 11.01 | AAA000 | −0.22 | 10.837 ± 0.005 | 10.788 ± 0.004 | 0.37 | 13.58 | 2.03 | 33.76 | 1.60 |
| 90..... | 7117 | 139 | 1.93 | 21.98 | 12.68 | 11.44 | 10.97 | AAA000 | −0.23 | ... | ... | 0.52 | 17.57 | 1.37 | 29.09 | 1.60 |
| 101..... | 10019 | 74 | 1.39 | 21.12 | 13.09 | 12.45 | 12.05 | AAA000 | 0.02 | ... | ... | 0.16 | 10.64 | ... | ... | 2.90 |
| 107..... | 9004 | 571 | 1.28 | 20.71 | 8.95 | 8.23 | 8.06 | AAA000 | −0.25 | 7.915 ± 0.003 | 7.923 ± 0.002 | 2.69 | 40.32 | 17.40 | 273.88 | ... |

Notes.—Cols. (1)–(5): COUP source number, source net counts, background counts within source's extraction region, source X-ray median energy, and inferred column density. All values are from Getman et al. (2005b). Cols. (6)–(8): VLT and 2MASS $JHK_s$ magnitudes as reported in Getman et al. (2005b). Col. (9): Flag indicating source of the NIR photometry ("..." = VLT; otherwise 2MASS) and quality of the 2MASS photometry as discussed in Getman et al. (2005b). Col. (10): Color excess measured from the rightmost reddening vector on the $J-H$ vs. $H-K_s$ color-color diagram (originating at $\sim$0.1 $M_\odot$ assuming an age of 1 Myr and using PMS models of Siess et al. 2000). Cols. (11)–(12): *Spitzer*-IRAC [3.6] and [4.5] magnitudes and their statistical errors obtained in this work. Cols. (13)–(14): Stellar mass and radius as listed in Getman et al. (2005b). Col. (15): Stellar rotation periods with extended rotation data for COUP sources as listed in Flaccomio et al. (2005). Col. (16): Calculated Keplerian corotation radius for stars with known $M$ and $P$. Col. (17): Equivalent width of the 8542 Å Ca II line as listed in Getman et al. (2005b). Table 3 is published in its entirety in the electronic edition of the *Astrophysical Journal*. A portion is shown here for guidance regarding its form and content.

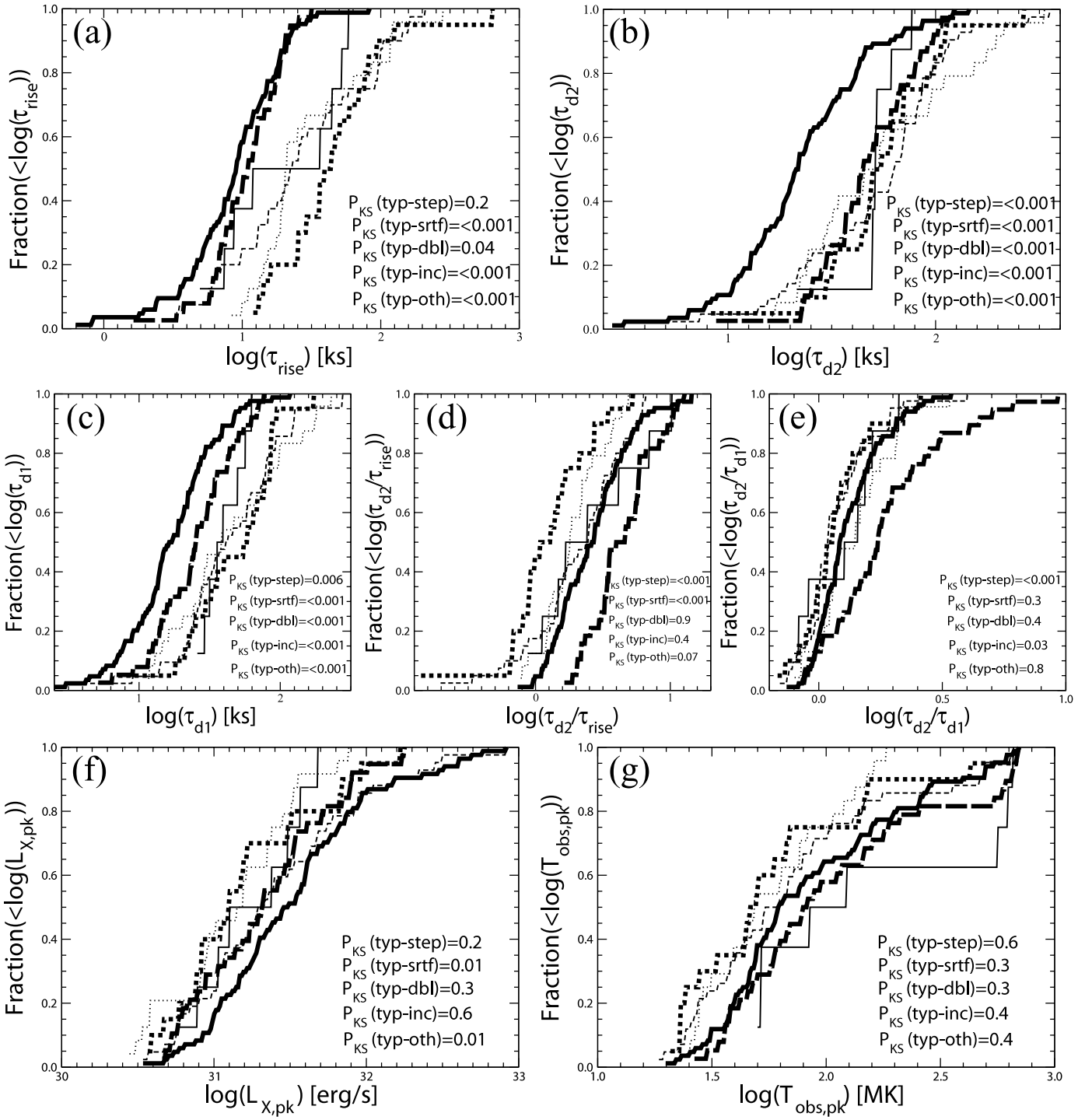


FIG. 7.—Cumulative distributions of flare properties: (*a*) rise time $\tau_{\rm rise}$, (*b*) decay time $\tau_{d2}$, (*c*) decay time $\tau_{d1}$, (*d*) ratio $\tau_{d2}/\tau_{\rm rise}$, (*e*) ratio $\tau_{d2}/\tau_{d1}$, (*f*) peak luminosity, and (*g*) peak temperature. Line types indicate morphological classes: 84 "typical" flares (*thick solid line*), 38 "step" (*thick dashed line*), 20 "srtf" (*thick dotted line*), 8 "double" (*thin solid line*), 42 "incomplete" (*thin dashed line*), and 24 "other" (*thin dotted line*). K-S probabilities test the assumption that "typical" and other flare types are drawn from the same underlying distribution.

rise is due to multiple heating events of a single magnetic loop, or a sequence of triggered reconnection events in a loop arcade. In contrast to all of these PMS flares, the rise time of the soft X-ray emission in a typical solar flare is typically only a few minutes (e.g., Priest & Forbes 2002), because solar chromospheric material fills the smaller solar flare volumes more quickly. Franciosini et al. (2007) provide statistics on rise and decay times for Taurus flares from the XEST study.

Figure 7*b* shows that the decay *e*-folding timescales derived over the whole flare interval, ($\tau_{d2}$), ranging from 3 hr to 1.5 days (10–150 ks) for 90% of the COUP flares. The median of $\tau_{d2} \sim 6$ hr (22 ks) for typical flares is much shorter than that of all other morphological flare classes, which have median decay times around 12 hr (~45 ks). The $\tau_{d1}$ decay timescales derived over the initial exponential decay phase $[t_{\rm CR,pk}-t_{\rm exp}]$ are on average a factor of 1.2 shorter than $\tau_{d2}$, again with decays

systematically shorter in typical flares than other classes (Figs. 7*c* and 7*e*). The decay timescales in typical solar flares are even shorter than or comparable to this, 10 minutes to a few hours (e.g., Reale et al. 1997; Priest & Forbes 2002). The ratios of rise and decay timescales serve as good quantitative discriminators between major different morphological flare classes. The median ratio $\tau_{d2}/\tau_{\rm rise}$ is 1.2, 2.6, and 4.3 ks for srtf, typical, and step flares, respectively (Fig. 7*d*). The median $\tau_{d2}/\tau_{d1}$ for step flares of 1.7 is much higher than the values of 1.1–1.2 for the typical, srtf, and other classes (Fig. 7*e*).

Figure 7*f* indicates that peak flare X-ray luminosities in the [0.5–8.0] keV band for our flare sample span $\log L_{\rm X,pk} \simeq 30.6$ to 32.3 erg s$^{-1}$ (90% range), with 10% of flares reaching luminosities $\log L_{\rm X,pk} \gtrsim 32$ erg s$^{-1}$. The strongest flare, flare 1 from COUP 1462, has a peak luminosity of 32.9 erg s$^{-1}$; it is also one of the hottest flares ($T_{\rm obs,pk} \gg 200$ MK). While the lower end of this distribution has no scientific importance due to our selection criteria, it is relevant that no significant luminosity differences are seen between different flare morphological classes, except for a possible indication that srtf flares do not achieve the highest peak luminosities. Similarly, no statistical differences in temperature distributions are seen (Fig. 7*g*). Temperatures span 20 to ~500 MK (90% range), with a median around 63 MK. Recall that individual values of temperatures above ~200 MK are quite uncertain (see Figs. 1 and 14*b*).

These results thus characterize the global properties of PMS flares with peak X-ray luminosities between 31 and 33 erg s$^{-1}$. The temperatures and luminosities of the brightest COUP flares are similar to the most luminous X-ray flares ever recorded in young stellar objects: V773 Tau in the Taurus clouds, with $L_{\rm pk} \gtrsim 10^{33}$ erg s$^{-1}$ and $T_{\rm pk} \gtrsim 100$ MK (Tsuboi et al. 1998), YLW 16A in the $\rho$ Ophiuchi Cloud, with $L_{\rm pk} \sim 2 \times 10^{32}$ erg s$^{-1}$ and $T_{\rm pk} \sim 140$ MK (Imanishi et al. 2001), LkH$\alpha$ 312 in the M78 reflection nebula of Orion, with $L_{\rm pk} \simeq 10^{32}$ erg s$^{-1}$ and $T_{\rm pk} \simeq 90$ MK (Grosso et al. 2004), and star 294 in the Cep OB3b region, with $L_{\rm pk} \simeq 2 \times 10^{32}$ erg s$^{-1}$ and $T_{\rm pk} \gg 100$ MK (Getman et al. 2006). Recall that even the most powerful solar flares today rarely exceed 28.5 erg s$^{-1}$ in the *Chandra* band.

While the differences between rise and decay timescales between our morphological classes mostly reflect our class definitions, the similarities in $L_{\rm X,pk}$ and $T_{\rm obs,pk}$ distributions among classes (Figs. 7*f* and 7*g*) are real results. They demonstrate that differences in flare morphology—particularly the difference between typical flares with fast rises and exponential decays and atypical flares with slow rises and flat tops—are not reflected in large differences in luminosity or temperature. This suggests that all types of flare morphologies arise from similar magnetic reconnection mechanisms.

### 3.2. *Comparison with Flares on Older Stars*

#### 3.2.1. *Comparison with General Solar-Stellar Scaling Law*

From their compilation and comparison of comprehensive data sets of solar and stellar[10] flares, Aschwanden et al. (2008) find a common scaling law between the peak flare emission measure ($\rm EM_{pk}$) and peak flare plasma temperature ($T_{\rm obs,pk}$), $\rm EM_{pk} \propto T_{obs,pk}^{4.7}$, but with stellar emission measures ~250 times higher than for solar flares. They also find that solar and stellar flare durations, $\tau_f$, follow the trend $\tau_f \propto T_{\rm obs,pk}^{0.9}$. For flare loop lengths, $L$, they find the trend $L \propto T_{\rm obs,pk}^{0.9}$ for solar flares only. Here we relate our 216 COUP flares to these scaling laws for solar-stellar flares.

[10] Stellar flare parameters for PMS and older active stars were taken from the compilation of Güdel (2004).

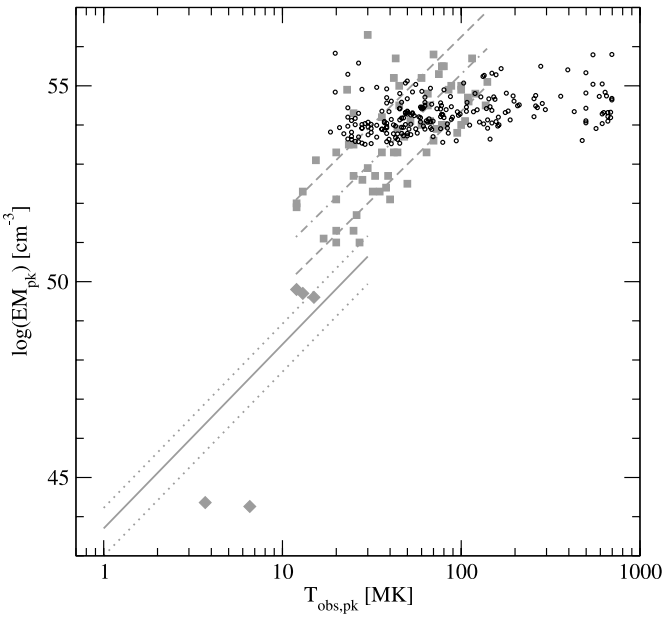


FIG. 8.—Plot of flare peak emission measure vs. peak temperature for different flare classes: 216 COUP flares (*black circles*), stellar flares compiled by Güdel (2004) (*gray boxes*) with their linear regression fit and 1 $\sigma$ ranges (*dashed-dotted and dashed lines*), and the regression fit to solar flares compiled by Aschwanden et al. (2008) (*solid and dotted lines*). Representative solar LDEs discussed in the text are shown as gray diamonds.

Figure 8 compares the $\rm EM_{pk}$-$T_{\rm obs,pk}$ relation between COUP flares (*black circles*), stellar flares of Güdel (2004; *gray squares*), and solar-stellar trends obtained by Aschwanden et al. (2008; *dashed and dotted lines*). The COUP flares represent the most luminous flare events ever detected from stellar objects, occupying the highest range in stellar emission measures, $53.5 < \log(\rm EM_{pk}) < 56$ cm$^{-3}$. The lower boundary corresponds to our selection cut of NC > 4000 source counts (§ 2.1).

In agreement with the scaling law of Aschwanden et al. (2008), about 60% of the COUP flares are located within the 67% range of flares from older stars (*dashed lines*). But the remaining stars do not follow the scaling law of Aschwanden et al. (2008): 34% (73 out of 216) of the COUP flares with unexpected superhot plasma temperatures of $T_{\rm obs,pk} \gtrsim 100$ MK strongly deviate from the expected $\rm EM_{pk} \propto T_{obs,pk}^{4.7}$ trend. These deviations may not be restricted to COUP flares; a careful examination of the stellar flare sample of Güdel (2004) shows that 10 out of their 11 flares (*gray squares*) with $T_{\rm obs,pk} \gtrsim 100$ MK are located below the regression line of Aschwanden et al. (2008), in agreement with the COUP superhot flares. Considered by themselves, the COUP flares follow a much shallower scaling law, $\rm EM_{pk} \propto T_{obs,pk}^{0.4}$. The statistical significance of this shallow correlation is strong: COUP flares with $T_{\rm obs,pk} < 100$ MK have median $\log(\rm EM_{pk}) = 54.09$ cm$^{-3}$, while superhot flares with $T_{\rm obs,pk} \gtrsim 100$ MK have a median $\log(\rm EM_{pk}) = 54.45$ cm$^{-3}$, with a two-sample probability of similar EM distributions $P_{\rm KS} \ll 10^{-4}$.

Figure 9 compares the flare duration $\tau_f$ to peak plasma temperature $T_{\rm obs,pk}$ for our COUP flares (*black circles*), stellar flares compiled by Güdel (2004; *gray squares*), and the regression fits for solar-stellar flares obtained by Aschwanden et al. (2008; *dotted lines*). Here we use our longest decay timescale $\tau_{d2}$ to correspond to their flare durations $\tau_f$. Flare durations for solar LDEs (long decay events; see § 3.2.2) are $\tau_f = (t_{\rm end} - t_{\rm start})$ on their *GOES* light curves, which are on average 3 times longer than their *e*-folding decay timescales.

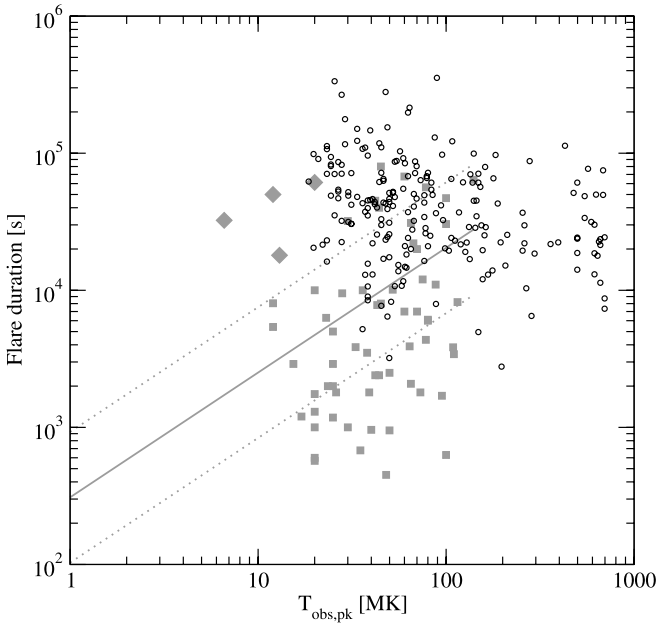


FIG. 9.—Plot of flare duration vs. flare peak temperature for different flare classes. Symbols and lines are as in Fig. 8.

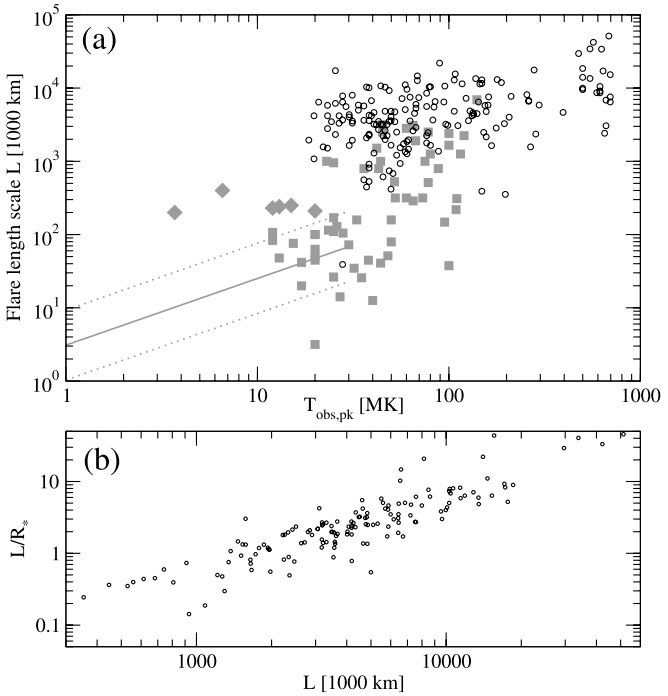


FIG. 10.—(*a*) Flare length scale vs. flare peak temperature for different flare classes. Symbols and lines are as in Fig. 8. (*b*) Comparison of inferred COUP flaring loop length to the loop length normalized by stellar radius ($L/R_\star$) for 147 COUP stars with known radii.

First, we note that the remarkably long duration (13 days) of the COUP observation provided a unique opportunity to capture stellar flares with decay timescales longer than a day. As in the $EM_{pk}$-$T_{obs,pk}$ plot, the COUP flares do not exhibit the reported solar-stellar relationship, $\tau_f \propto T_{obs,pk}^{0.9}$. While some COUP flares studied here are consistent with the relation, the majority deviate strongly, with peak plasma temperatures either too cool or too hot. For COUP flares, we find a weak trend in the other direction, $\tau_{d2} \propto T_{obs,pk}^{-0.2}$. Similar results are obtained using our flare rise timescale $\tau_r$ and initial flare decay timescale $\tau_{d1}$, and the trends are confirmed with Kolmogorov-Smirnov tests.[11] The median duration for flares with $T_{obs,pk} < 100$ MK is $\tau_{d2} = 45$ ks, compared to 25 ks for superhot flares with $T_{obs,pk} \gtrsim 100$ MK. However, here we do not analyze many hundreds of weaker and shorter COUP flares that could potentially compensate for some of these deviations.

Although stellar and COUP flare loop lengths are derived from cooling models rather than directly from the observations, it is useful to compare COUP, stellar, and solar length distributions. Figure 10*a* shows the COUP flares (*black circles*), stellar flares (*gray squares*), and the loci of solar flares (*dotted lines*) in the $L$-$T_{obs,pk}$ diagram. For COUP flares, $L$ is the mean value of the inferred $[L_1 - L_2]$ range. COUP loop sizes range from $<10^{11}$ cm to $\gtrsim 10^{12}$ cm, a range of very large loops previously occupied by only dozen stellar flares. These loop sizes are $10^2$–$10^3$ larger than seen in solar flares. Figure 10*b* shows that the variables $L$ and $L/R_*$ are roughly equivalent; COUP flare loop lengths range from $\sim$0.2 to $\gtrsim$10 stellar radii. COUP loop lengths slowly increase with peak flare temperature, roughly as $L \propto T_{obs,pk}^{(0.4-0.5)}$, consistent with the slope seen in solar flares but offset to much larger lengths at a given temperature. This trend, however, emerges from the assumptions underlying our loop modeling (§ 2.3, eqs. [1] and [3]), and thus may not be physically significant.

We thus find that flares in our COUP sample are indeed among the most luminous, hottest, largest (in term of loop length), and most long-lived of any X-ray flares known. Comparison with the stellar-solar scaling laws of Aschwanden et al. (2008) provides nontrivial results. One-third of the COUP sample have superhot temperatures of $T_{obs,pk} > 100$ MK. These do not fit the strong $EM_{pk} \propto T_{obs,pk}^{4.7}$ solar-stellar scaling law; rather, in the COUP regime, temperatures can increase several fold above 100 MK with only slight increase in plasma emission measures. This may be related to the low efficiency of filling up very large coronal loops of PMS stars with hot plasma from chromospheric evaporation. COUP flares also do not follow the solar-stellar correlation between flare duration and peak plasma temperature; indeed, we find a slight antitrend, where hotter COUP flares are on average slightly shorter in duration than cooler flares. However, a previously reported correlation between flare loop length and peak plasma temperature is present, although offset to longer loops than seen in solar and older stellar flares. Further analysis of COUP superhot flares is presented in Paper II.

Some form of saturation of previously reported relationships is clearly present. Unlike solar flares, which arise in small-scale multipolar fields, COUP flaring magnetic structures are typically larger than the radii of their host stars. We turn now to possible relationships with a rare class of long-duration solar flares that are also believed to be associated with large-scale coronal structures.

#### 3.2.2. *Solar Long-Decay Flare Events*

Giant X-ray arches and streamers with altitudes reaching up to several hundred thousand kilometers produced during some solar flares have been observed by the *Skylab*, *SMM*, and *Yohkoh* space observatories (Hiei 1994; Švestka et al. 1995; Farnik et al. 1996; Švestka et al. 1997; Hiei 1997 and references therein). Such events were originally called long-decay events (LDEs; Kahler 1977). Corresponding X-ray light curves of solar LDEs often exhibit flares lasting from a few hours to a day, similar to flare durations in our sample. Figure 11 shows the *GOES* light

[11] KS results indicate significant differences between distributions of $\tau_r$ ($P_{KS} = 0.004$) with median values of $\tau_r = 15.8$ and 9.7 ks for $T_{obs,pk} < 100$ and $\gtrsim 100$ MK flares, respectively; and $\tau_{d1}$ ($P_{KS} = 0.001$) with median values of $\tau_{d1} = 30.1$ and 21.5 ks for $T_{obs,pk} < 100$ and $\gtrsim 100$ MK flares, respectively.

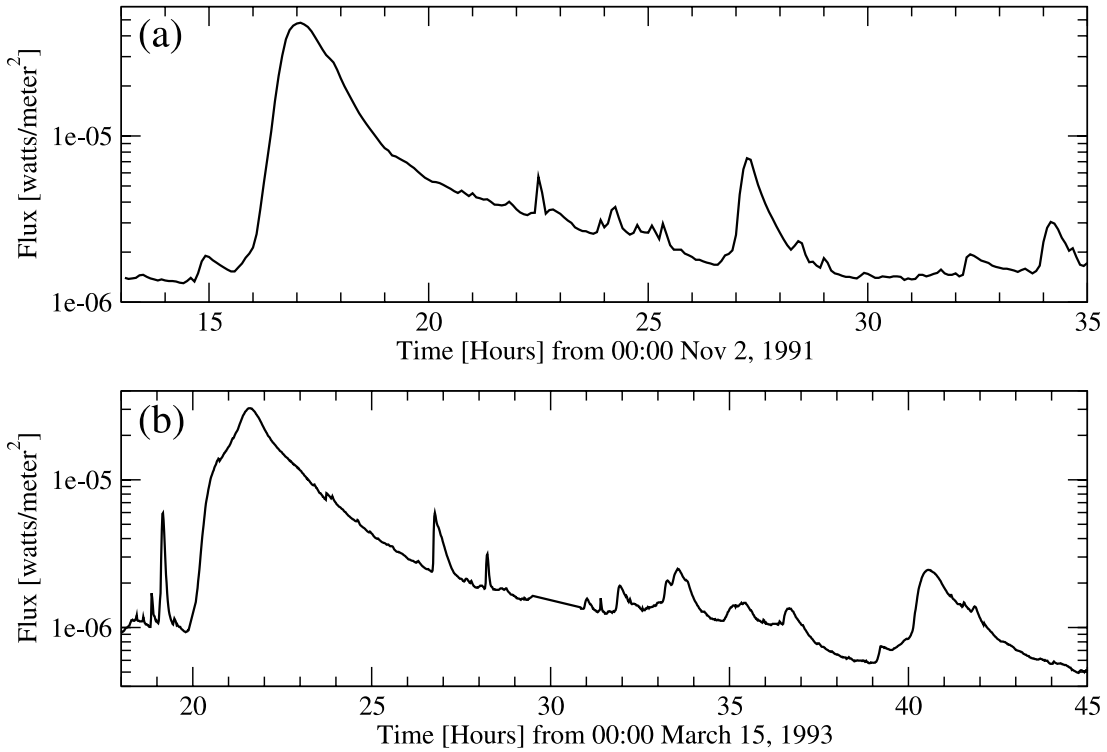


FIG. 11.—X-ray light curves obtained in the 1–8 Å band by *GOES* during the formation of giant solar X-ray arches (Švestka et al. 1995) on (*a*) 1991 November 2 and (*b*) 1993 March 15.

curves of long solar flares associated with giant X-ray arches. The origin of solar X-ray giant arches and streamers is not well understood. One popular model suggests that the powerful prominence eruption or coronal mass ejection, often (but not always) associated with an impulsive flare (Priest & Forbes 2002), expands into an overlying large-scale magnetic field, with the subsequent reconnection of magnetic lines through a vertical current sheet and formation of a system of giant closed loops in the shape of arches and streamers (Sturrock 1966; Kopp & Pneuman 1976; Forbes & Acton 1996).

Flare parameters for a number of solar LDEs are shown in Figures 8–10 (*gray diamonds*).[12] Peak emission measures of solar LDEs vary from $\log(\mathrm{EM_{pk}}) \sim 44$ cm$^{-3}$ for X-ray streamers to $\log(\mathrm{EM_{pk}}) \sim 50$ cm$^{-3}$ for giant arches, with flare durations $\tau_f >$ 10 ks and altitudes of $L \gtrsim 1 \times 10^{11}$ cm. Both durations and altitudes are well above the loci of typical solar flares. In addition, several solar flare limb events observed by *Skylab* with inferred durations of >12,000 s, temperatures of >7–8 MK, and altitudes of $>3$–$4 \times 10^{10}$ cm, which are called Class II events (Pallavicini et al. 1977), are also located far the usual solar flare locus (see diamond symbols in Fig. 4 of Aschwanden et al. 2008). These may represent a subclass of solar LDEs.

With their extremely long flare durations, often hot temperatures, and associated large-scale flaring structures, LDEs are thus outliers from the solar flare scaling laws, similar in many respects to the COUP flares analyzed here. It is reasonable to propose that the majority of the flares in our COUP flare sample are enhanced analogs of these solar LDEs. Concerns regarding possible effects of centrifugal forces and magnetic field confinement on the COUP PMS flares are discussed in Paper II.

[12] Flare parameters are presented for the following solar LDEs: giant arches observed on 1991 November 2 and 4, 1992 February 21, and 1993 March 15; X-ray streamers seen on 1992 January 24 and October 28. Peak flare emission measures, plasma temperatures, and maximum altitudes are taken from Švestka et al. (1995, 1997) and Getman & Livshits (2000). Flare durations are $\tau_f = (t_{\mathrm{end}} - t_{\mathrm{start}})$ in their *GOES* light curves.

## 4. CONCLUSIONS

We analyze 216 bright X-ray flares from the Chandra Orion Ultradeep Project, which provides the longest nearly continuous observation of a rich PMS stellar cluster in the X-ray band. Our effort is based on a new spectral analysis technique (MASME) that avoids nonlinear parametric modeling and is more sensitive than standard methods. Flare loop parameters are derived from the well-established flare plasma model of Reale et al. (1997).

We thus emerge with the largest data set of PMS flares, or indeed stellar flares at any stellar age, with peak luminosities in the range $31 < \log L_{\mathrm{X,pk}} < 33$ erg s$^{-1}$, several orders of magnitude more powerful than any solar flare. For each flare we provide a catalog of >30 derived flare properties, including inferred sizes of associated coronal loops and flare morphological classes. In Figure Set 2 we give an atlas with flare light curves, temporal evolution plots of the X-ray median energy, plasma temperature, emission measure, and derived temperature density diagram. This collection of empirical and model-dependent information can serve as a valuable testbed for stellar flare models.

The powerful COUP flares studied here have rise timescales ranging from 1 hr to 1 day, and decay timescales ranging from a few hours to 1.5 days. An important empirical result is that peak plasma temperatures are often 100 MK, in some cases >200 MK. These temperatures are derived from a robust calibration of median energies; traditional time-resolved spectroscopy often does not have the time resolution to detect this brief superhot phase. No significant differences in peak flare luminosity or temperature distributions are found among the wide range of morphological flare classes: typical fast-rise exponential decays, step decays, double peaks, and slow-rise flat top. This suggests that

all flare types arise from similar underlying magnetic reconnection mechanisms and geometries.

Comparison of the COUP flare properties with the general solar-stellar scaling laws of Aschwanden et al. (2008) presents surprising results. Our flares do not follow the solar-stellar trend between plasma peak emission measure and temperature, $EM_{pk} \propto T_{obs,pk}^{4.7}$. The trend between flare duration and peak temperature is also absent. Superhot COUP flares are found to be brighter but shorter in duration than cooler COUP flares. This is further developed in Paper II.

Compared to non-PMS systems, the inferred sizes of COUP flaring structures are remarkably large, ranging widely from $L = 0.5$ to 10 $R_\star$. These large flaring structures must be associated with large-scale stellar magnetic fields. Rare long-decay solar events associated with the largest known X-ray-emitting structures are possible solar analogs to these COUP flares.

Our flare sample provides a valuable laboratory for the study of the physics and astronomy of magnetic reconnection events. This study (Paper I) examines flare morphologies, and provides a general comparison of COUP flare characteristics with those of other active X-ray stars and the Sun. Paper II concentrates on relationships between flare behavior, protoplanetary disks (both passive and accreting), and other stellar properties, including rotational periods and Keplerian corotation radii. Paper II further investigates superhot COUP flares and magnetic field strength on Orion T Tauri stars.

K. G. thanks Moisey Livshits for introducing him to the physics of solar long-decay events. We thank Vinay Kashyap, Rachel Osten, and Paola Testa for the stimulating discussions, and Kevin Luhman for assistance with *Spitzer*-IRAC data analysis. We also thank the referee, Jeffery Linsky, for his time and many useful comments that improved this work. This work was supported by the *Chandra* ACIS Team (PI: G. Garmire) through the SAO grant SV4-74018. G. M. acknowledges contribution from contract ASI-INAF I/088/06/0. This publication makes use of data products from the Two Micron All Sky Survey (a joint project of the University of Massachusetts and the Infrared Processing and Analysis Center/California Institute of Technology, funded by NASA and NSF), and archival data obtained with the *Spitzer Space Telescope* (operated by the Jet Propulsion Laboratory, California Institute of Technology under a contract with NASA).

## APPENDIX A

## COMPARISON OF MASME WITH TIME-RESOLVED SPECTROSCOPY

Studies of stellar flare evolution have been conducted for some years using low spectral resolution time series characteristic of CCD detectors on the *ASCA*, *Chandra*, *XMM-Newton*, and *Suzaku* satellites. Most of these studies have used a method we call time-resolved spectroscopy (TRS), where the light curve is divided into intervals (e.g., flare rise, flare peak, and several flare decay intervals), and full multiparameter fits to the spectra are made in each interval. These fits are typically made with a code such as XSPEC (used here and throughout the COUP effort), Sherpa, or MIDAS, with the assumption of a one- or two-temperature plasma subject to absorption. In the case of very high signal, nonsolar elemental abundances may also be added as free parameters. Examples of such analyses applied to powerful PMS stellar flares include the reheated flare of the weak-lined T Tauri star V773 Tau in the Taurus clouds seen with *ASCA* (Tsuboi et al. 1998), the complex flare of the protostar YLW 16A in the Ophiuchi cloud seen with *Chandra* (Imanishi et al. 2001), the slow-rise flare of the weak/classical T Tauri star LkH$\alpha$ 312 in the Orion B cloud seen with *Chandra* (Grosso et al. 2004), the strong flare in the Herbig Ae star V892 Tau in Taurus clouds seen with *XMM-Newton* (Giardino et al. 2004), 18 more brightest flarelike events from T Tauri stars in Taurus clouds analyzed in the XEST project

TABLE 4
TIME-RESOLVED SPECTROSCOPY ANALYSIS

| Source (1) | Flare No. (2) | Type (3) | SegNum (4) | $\langle N \rangle_{seg}$ (counts) (5) | $N_{char}$ (counts) (6) | $T_{char}$ (MK) (7) | $T_{pk,TRS,noCH}$ (MK) (8) | $T_{pk,TRS,CH}$ (MK) (9) | $\zeta_{TRS,noCH}$ (10) | $\zeta_{TRS,CH}$ (11) |
|---|---|---|---|---|---|---|---|---|---|---|
| 7..... | 1 | typ | 8 | 202 | 1458 | 12.69 | 37.11 | 37.48 | 1.14 | 0.95 |
| 9..... | 1 | inc | 9 | 261 | 484 | 16.02 | 66.01 | 66.54 | −0.10 | −0.12 |
| 11..... | 1 | stp | 6 | 152 | 194 | 12.21 | 927.22 | 927.22 | 2.13 | 2.09 |
| 23..... | 1 | typ | 12 | 333 | 2090 | 16.16 | 53.72 | 54.10 | 1.15 | 0.99 |
| 27..... | 1 | inc | 3 | 80 | 175 | 12.10 | 32.50 | 33.61 | 1.51 | 1.38 |
| 27..... | 2 | stp | 11 | 130 | 175 | 12.10 | 45.83 | 50.22 | 0.67 | −0.49 |
| 28..... | 1 | inc | 22 | 586 | 381 | 15.76 | 59.45 | 59.48 | 0.69 | 0.67 |
| 43..... | 1 | srf | 8 | 208 | 210 | 15.96 | 74.90 | 77.30 | 2.09 | 2.15 |
| 57..... | 1 | dbl | 5 | 136 | 115 | 12.74 | 43.64 | 46.88 | 2.00 | 1.91 |
| 57..... | 2 | oth | 3 | 76 | 115 | 12.74 | 29.60 | 61.54 | −1.88 | −2.89 |
| 62..... | 1 | oth | 13 | 273 | 149 | 29.90 | 39.97 | 40.42 | 0.79 | 0.74 |
| 62..... | 2 | typ | 4 | 172 | 149 | 29.90 | 68.25 | 71.53 | 2.15 | 1.87 |
| 66..... | 1 | dbl | 5 | 160 | 155 | 11.29 | 77.00 | 77.97 | 1.24 | 1.16 |
| 67..... | 1 | typ | 4 | 145 | 227 | 12.97 | 41.94 | 45.77 | 1.96 | 0.49 |
| 71..... | 1 | stp | 9 | 276 | 113 | 10.95 | 43.10 | 46.87 | 1.89 | 0.56 |

NOTES.—Cols. (1)–(3): Source number, flare number, and flare morphological type (reproduced from Table 2). Cols. (4)–(5): Number of segments and the average number of X-ray counts per segment used in the TRS analysis. Cols. (6)–(7): Number of X-ray counts in the "characteristic" segment and inferred "characteristic" plasma temperature. Cols. (8)–(9): Inferred peak flare plasma temperatures without ("noCH") and with ("CH") account for the "characteristic" background. Cols. (10)–(11): Inferred average slopes of the temperature-density trajectory without ("noCH") and with ("CH") accounting for the "characteristic" background. Table 4 is published in its entirety in the electronic edition of the *Astrophysical Journal*. A portion is shown here for guidance regarding its form and content.

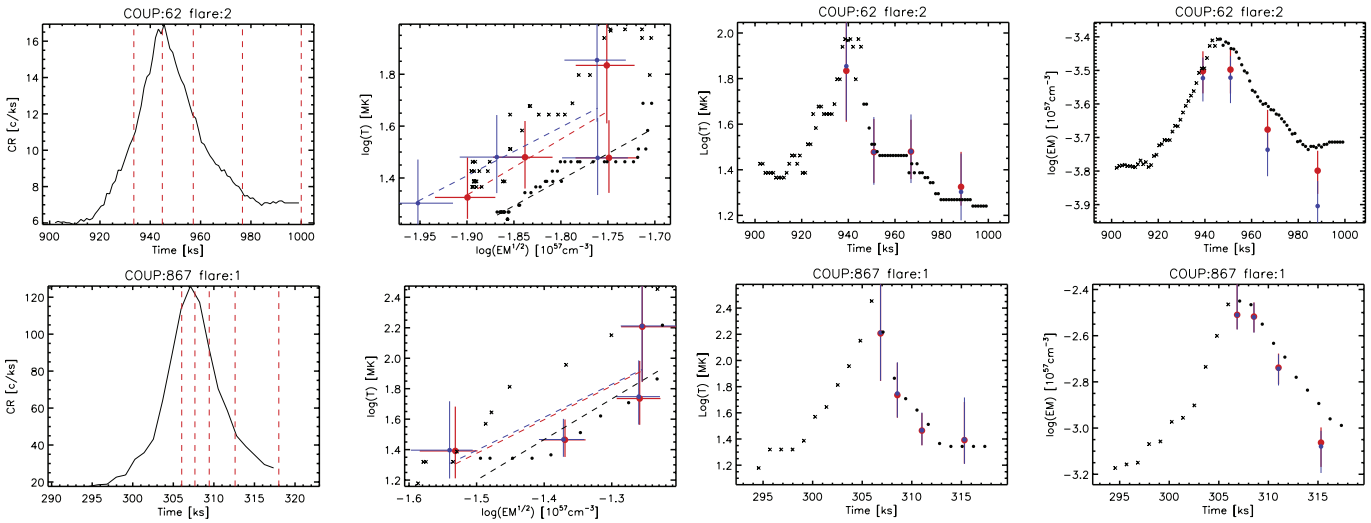


FIG. 12.—Comparison of MASME and TRS flare analyses for representative "typical" flares with four TRS segments. Each source is represented by four panels (*left to right*): adaptively smoothed light curve with dashed red lines indicating TRS segments, $\log(T)-\log(\mathrm{EM}^{1/2})$ diagram, temporal evolution of plasma temperature, and temporal evolution of emission measure. Black circles (crosses) indicate MASME-derived decay (rise) points. Blue (red) circles with error bars are TRS-derived points for the peak-decay light curve phase with (without) accounting for the "characteristic" background. Dashed lines are linear regressions to MASME points over the whole decay phase (*black*; denoted as slope $\zeta_1$ in Table 2) and to TRS points over the peak-decay phase (blue and red for the "CH" and "noCH" cases, respectively).

(Franciosini et al. 2007), and the study of 32 powerful Orion Nebula Cluster flares in Orion A based on COUP data (Favata et al. 2005).

The main difference between our MASME method and the TRS method is that we obtain the temperature and emission measure evolutions on rapid timescales directly from the smoothed median energy and count rate evolutions, without using a fitting procedure for analyzed data (§ 2.2). The calibration curves shown in Figure 1 are crucial for converting median energies to plasma temperatures. This permits estimation of temperature and emission measure (luminosity) at many more time points using fewer counts at each time step than possible with TRS. No fitting based on least-squares or maximum likelihood statistical procedures is made. Drawbacks to MASME include the omission of characteristic level emission and the inability to track possible $N_{\mathrm{H}}$ variations; note that these capabilities of TRS are also neglected in many previous studies.

To compare the two methods, we have conducted a TRS analysis of the 216 COUP flares, as follows. We examine the consistency of the two procedures, and examine the effects of neglecting the characteristic emission. The peak plus decay interval of each flare is divided into a number of segments (SegNum), each hosting a roughly constant number of X-ray flare counts ($\langle N \rangle_{\mathrm{seg}}$). For the majority of flares (∼54%), we defined ≥5 segments with ∼200 counts each. For weaker flares (∼28%), we defined ≳3 segments with 100 to 200 counts each. For the brightest flares (18%), we defined ≳10 segments with ≳300 counts each.

Table 4 presents the results of the TRS analysis including information on light curve segmentation, "characteristic" background spectrum, inferred flare peak temperatures, and temperature-density slopes. Several "typical" flares with simple single-decay

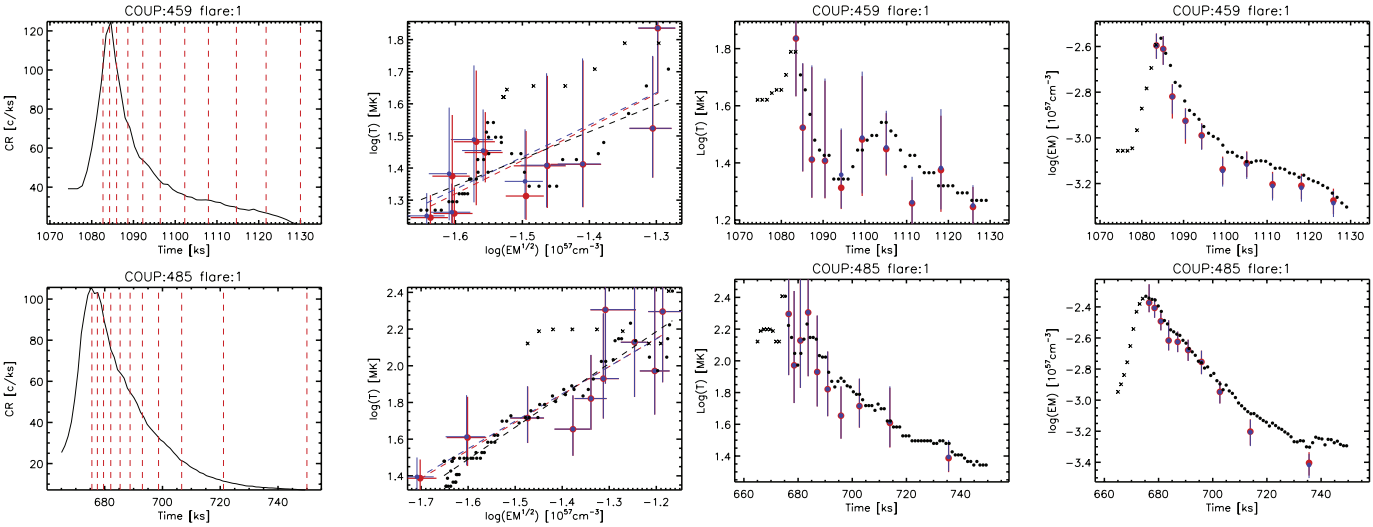


FIG. 13.—Comparison of MASME and TRS flare analyses for representative "typical" flares with 10 TRS segments. See Fig. 12 for details.

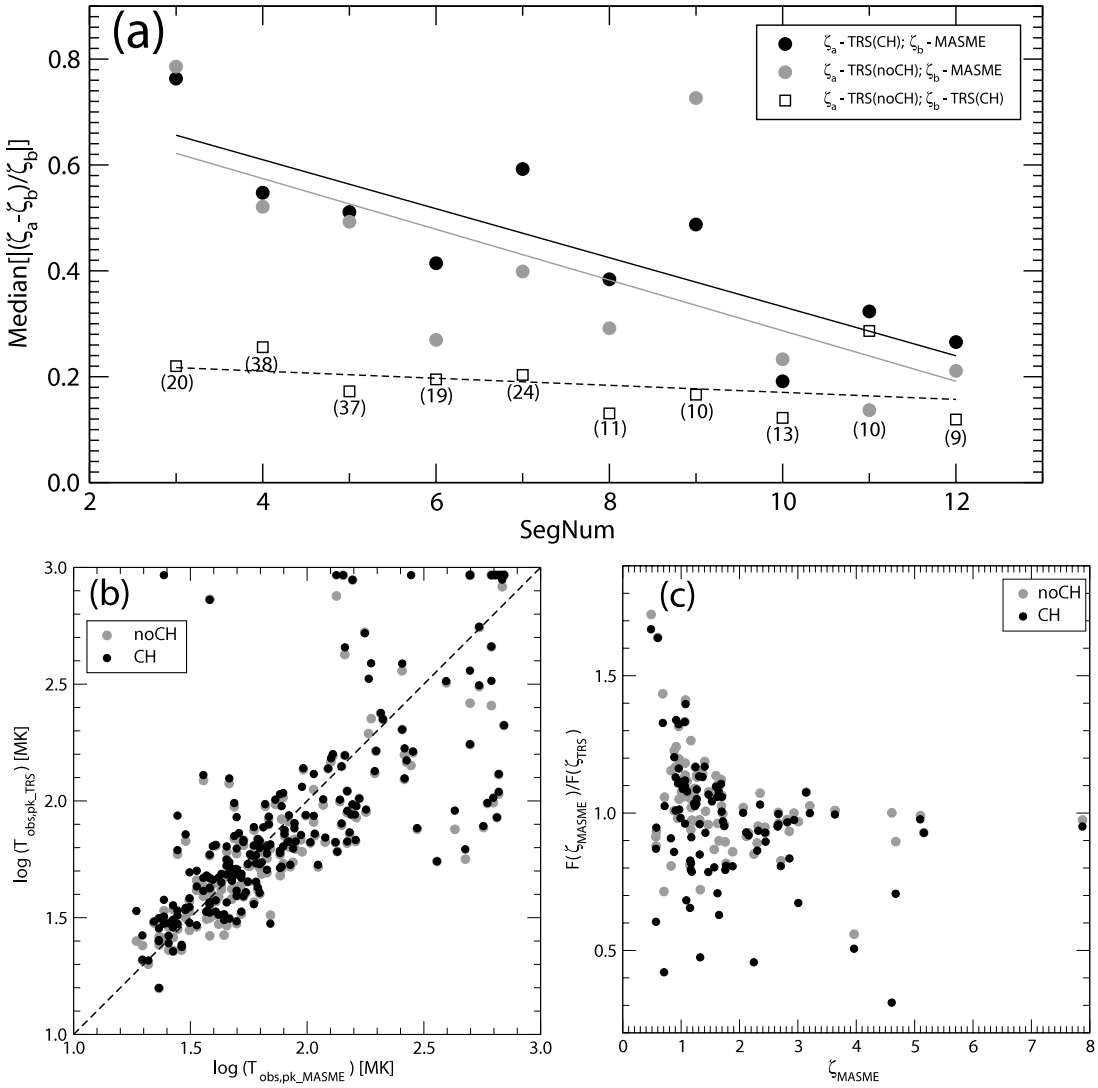


FIG. 14.—Comparison of MASME and TRS flare analyses results. (*a*) Median fractional difference between inferred slopes in the log ($T$)– log (EM$^{1/2}$) diagram as a function of number of TRS segments. Black circles indicate correction for "characteristic" background emission ("CH"), while gray circles indicate no correction ("noCH"). Open boxes indicate median fractional difference between TRS "CH" and TRS "noCH." Lines represent linear regressions of the data points. Numbers in parentheses report the number of flares that have the specified number of TRS segments. (*b*) Comparison between MASME- and TRS-inferred peak flare temperatures. (*c*) Ratio of the MASME to TRS correction factors $F(\zeta)$ for prolonged heating (see § 2.3) vs. the MASME slope.

slopes are presented in Figures 12 and 13. Results are provided for cases with ("CH") and without ("noCH") accounting for the characteristic nonflare emission. The spectrum of each segment is fitted with the WABS × MEKAL model (compatible with previous COUP spectroscopic fits; Getman et al. 2005b), plus a similar model of the characteristic component in the "CH" cases. The absorption $N_H$ is frozen to the value obtained from the global fits of Getman et al. (2005b), and 0.3 times solar elemental abundances are assumed. The characteristic spectrum was obtained from the $[t_{char1}–t_{char2}]$ segment, which is the >20 ks light curve block with the least median value of the count rate. There is, of course, no guarantee that the characteristic emission is the same during the flare interval.

Figure 14 compares several outcomes of the MASME technique with those of TRS. Figure 14*a* shows that the inferred TRS slopes of the trajectories in the log ($T$)– log (EM$^{1/2}$) diagram which omit the characteristic emission ($\zeta_{TRS,noCH}$) are systematically steeper by $\simeq$20% to $\simeq$15% with increasing number of TRS segments than those that account for characteristic emission ($\zeta_{TRS,CH}$; see open boxes and the dashed regression line in Fig. 14*a*). This arises because the flare spectrum is generally harder than the characteristic spectrum.

There is no strong systematic difference in slope steepness when TRS is compared to MASME: in $\sim$45% ($\sim$60%) of all flares the inferred average MASME slopes ($\zeta_1$ from Table 2) are steeper than the TRS slope $\zeta_{TRS,noCH}$ ($\zeta_{TRS,CH}$). The MASME-TRS slope difference is quite high ($\sim$50%–65%) for generally weak flares with only few TRS segments, but decreases to $\sim$20%–30% for generally brighter flares with the number of TRS segments $\gtrsim$10 (black and gray circles and lines in Fig. 14*a*). We believe that the major reason for the observed MASME-TRS slope difference is not the presence or absence of the "characteristic" background, which contributes only a few percent to the difference (offset between the gray and black lines), but is rather due to the poor sampling of the temperature-density trajectory slope by the TRS method when only few TRS segments are available in the case of weak flares.

Figure 14*b* shows that the peak flare temperatures $T_{pk,TRS,noCH}$ and $T_{pk,TRS,CH}$ obtained from the TRS method are essentially the same, and MASME vs. TRS temperature differences are within 20%. A 20% difference in temperature corresponds to a <20%

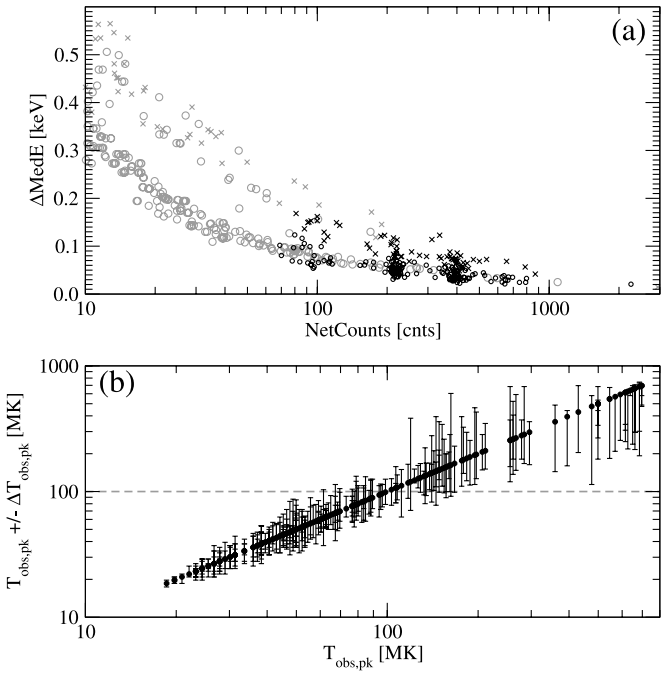


FIG. 15.— Validation of median energy and peak temperature estimates. (*a*) Comparison between 1 $\sigma$ errors on median energy obtained from Monte Carlo simulations of Cepheus B X-ray sources (*gray symbols*; from Getman et al. 2006) and errors derived from the MAD technique applied to COUP flaring sources (*black symbols*). Circles indicate Med $E < 2$ keV, and crosses indicate Med $E > 2$ keV. (*b*) Errors on peak flare plasma temperature derived for our COUP flare sample, based on the median energy calibration curve in Fig. 1. Upper errors on $T_{\rm obs,pk} \gtrsim 300$ MK are unreliable, due to the lack of calibration data points above 700 MK.

difference in estimated loop sizes. Large scatter in temperatures are seen for $T \gtrsim 200$ MK; this inability to quantify very high plasma temperatures is expected given the 8 keV high-energy limit and low high-energy sensitivity of *Chandra* spectra.

Figure 14*c* examines MASME vs. TRS estimates of the correction factors associated with flare prolonged heating or triggered flare events [the factor $F(\zeta)$ presented in § 2.3]. This comparison is restricted to 108 flares with a single average decay slope $\zeta_1$ (i.e., flares with $\rm Flag_1 = 01$ in Table 2). Here again, the two methods generally agree within 20%.

We emerge with considerable confidence in the MASME approach. Except for temperatures $T \gtrsim 200$ MK, basic physical flare properties such as temperature, emission measure, and luminosity evolution are essentially the same using the TRS and MASME methods. Flare model parameters such as reheating corrections and loop sizes are also reproduced. A reasonable estimate for the precision of loop sizes is <40%, understanding that the underlying model of Reale et al. (1997) may not be adequate for understanding the more complex flares. The advantage of the MASME method is its ability to treat weaker and more rapidly variable flares than TRS. In the case of COUP, we are able to study >6 times more flares than could be studied using TRS by Favata et al. (2005).

## APPENDIX B

## ERROR ANALYSIS OF MASME SPECTRAL MODELING

Here we describe our estimation procedure of statistical and systematic errors on peak flare plasma temperature in our MASME modeling. This is important both for estimating magnetic loop sizes and for identifying superhot flares. We use the median absolute deviation (MAD) normalized by $0.6745/\sqrt{(N)}$,

$$\Delta{\rm Med}E = {\rm median}|E_i - {\rm Med}E|/\left[0.6745/\sqrt{(N)}\right] \quad \text{(B1)}$$

where $|\ldots|$ indicates absolute value, and $E_i$ is the energy of each of the $N$ X-ray photons appearing within the sliding boxcar kernel used to calculate peak flare median energy Med$E$. The MAD is a well-established estimate of the uncertainty of the median, which is scaled to the standard deviation when the distribution is Gaussian (Beers et al. 1990).

Figure 15*a* compares errors on median energy estimated using Monte Carlo simulations for flaring PMS stars in the Cepheus B region (*gray symbols*; from Getman et al. 2006) with errors on COUP peak flare median energy (*black symbols*) obtained with the simple MAD formula above. There is a perfect match between the two completely different methods of error analysis, even for different Med$E$ strata (circles vs. crosses).

The errors on peak flare plasma temperature are shown in Figure 15*b*. They are derived through propagation of errors on peak flare Med$E$ using the simulation-based $T_{\rm obs,pk}$–Med$E$ calibration curves (Fig. 1). Upper errors for many sources with $T_{\rm obs,pk} \gtrsim 300$ MK are unreliable due to the lack of calibration data above 700 MK (Fig. 1). Lower 1 $\sigma$ errors are generally <20% for $T_{\rm obs,pk} < 50$ MK, <30% for $T_{\rm obs,pk} < 100$ MK, <40% for $T_{\rm obs,pk} < 200$ MK, and ~60% for the hottest flares.

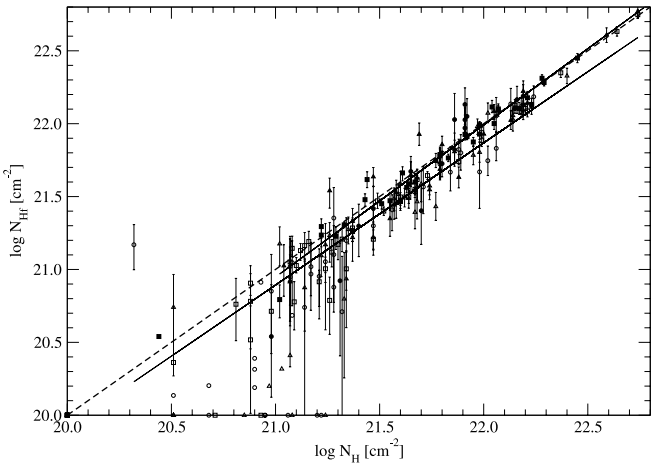


FIG. 16.—Comparison of column densities derived here from fits of flare spectra, $N_{\rm Hf}$, with column densities (Getman et al. 2005b) derived from fits of time-integrated COUP spectra (within the whole COUP observation), $N_{\rm H}$. Symbols represent different flare counts: circles ($NC_f < 1000$), triangles ($1000 < NC_f < 2000$) and squares ($NC_f > 2000$). Filled symbols denote 73 superhot flares. The dashed line shows values of $\log(N_{\rm Hf}) - \log(N_{\rm H}) = 0$. The shorter solid line is a regression line to all superhot flares with known formal statistical errors on $N_{\rm Hf}$ (*vertical bars*). The longer solid line is a regression line to all cooler flares with known errors.

We now further consider how uncertainties of inferred X-ray column densities may affect the errors of derived flare peak plasma temperatures shown in Figure 15*b*. First, it is important to note that 89% of superhot flares (compared to 50% for cooler flares) are found in stars for which the inferred X-ray column densities are $\log N_{\rm H} > 21.3$ cm$^{-2}$ (Fig. 16). This indicates that the superhot flares are not the result of some data analysis bias, such as an effect of a systematic underestimate of $N_{\rm H}$, but rather relate to real physical phenomena connected to actively accreting disks around young stars, as is shown in Paper II.

Second, because the studied COUP stars are extremely strong sources with thousands of counts, statistically, their $\log N_{\rm H}$ is measured with very high accuracy. Formal statistical uncertainties are less than $\pm 0.03$ dex ($1\,\sigma$) for sources with $\log N_{\rm H} > 21.2$ cm$^{-2}$, and less than $\pm 0.07$ dex for most of the softer COUP sources. Such statistical errors on $N_{\rm H}$ have only marginal effects on the resulting temperature errors. For example, in a representative case of a superhot flare from the COUP source 1309 with $\log N_{\rm H} = 22.00 \pm 0.02$ cm$^{-2}$, the propagation of statistical errors on $N_{\rm H}$ will change the errors on plasma temperature of $T_{\rm obs,pk} = 188^{+75}_{-67}$ MK shown in Figure 15*b* from 40% to 53% and from 36% to 43% of an inferred mean temperature value for the upper and lower error limits, respectively. For a representative case of a cooler flare from COUP source 1492 with $\log N_{\rm H} = 21.07 \pm 0.05$ cm$^{-2}$, its errors on a temperature of $T_{\rm obs,pk} = 51^{+21}_{-19}$ MK will change from 41% to 50% and from 37% to 38%, for the upper and lower error limits, respectively.

However, for the group of 8 extremely soft sources[13] with their reported $\log N_{\rm H}$ values truncated at 20.0 cm$^{-2}$, the spectral model assumed by Getman et al. (2005b) used to derive $\log N_{\rm H}$ (two plasma MEKAL temperatures with 0.3 times solar elemental abundances with Wisconsin gas absorption) is not sufficiently complex to fit the observed spectra well around the O VII and O VIII emission line complex. This is because spectral lines are present from FIP-related abundance anomalies that are not in the Getman et al. spectral model. These abundance effects are documented in detail by Maggio et al. (2007) for nearly the same sample of bright COUP stars as we analyze here. We refitted these 8 extremely soft spectra with two-temperature component VMEKAL models with individual elemental abundances as free parameters to obtain statistically good spectral fits. In accord with the results of Maggio et al., who used VAPEC models, we find that while for some of these spectra (sources 71, 597, 1481) the formal $\log N_{\rm H}$ reported by XSPEC continue to be less than 20.0, for others the inferred $\log N_{\rm H}$ may increase to 20.5–20.7 cm$^{-2}$. In the former cases, our calibration curves in Figure 1 assuming $\log N_{\rm H} = 20.0$ cm$^{-2}$ will not change, due to the insensitivity of ACIS-I spectra to very low column densities. In the latter cases, the shift from $\log N_{\rm H} = 20.0$ to 20.5–20.7 cm$^{-2}$ only slightly affects the lower error limits on peak flare plasma temperatures, which are typically around 30 MK. For example, the lower error on the plasma temperature $T_{\rm obs,pk} = 27^{+7}_{-6}$ MK of source 1595 will change only from 22% to 26% of an inferred mean temperature value when a shift from $\log N_{\rm H} = 20$ cm$^{-2}$ to the newly inferred 20.5 cm$^{-2}$ is applied.

Time-integrated COUP spectra are typically several times stronger than spectra of individual flares. To take advantage of this fact in our flare analysis, we fixed column densities to $N_{\rm H}$ values derived from the two-temperature fits of time-integrated COUP spectra (Getman et al. 2005b). To verify whether this produces a source of systematic uncertainty on column density, flare spectra were extracted within flare time range of $[t_{\rm flare1}-t_{\rm flare2}]$ and fitted by one-temperature WABS×MEKAL model with 0.3 times solar abundances allowing both temperature and column density to be free parameters. Figure 16 compares column densities resulted from these flare fits, $N_{\rm Hf}$, with column densities from time-integrated fits, $N_{\rm H}$, showing no systematic differences in the case of superhot flares (shorter solid regression line vs. dashed line), but suggesting that $N_{\rm H}$ can be systematically overestimated by $\sim$0.12 dex in the case of "cooler" flares (longer solid regression line vs. dashed line). This has only a marginal effect on the resulting temperature errors. For example, in a representative case of a "cooler" flare from COUP source 1492 considered above, this systematic shift will only change the temperature upper limit from 50% to 55% of an inferred mean temperature value of 51 MK.

Finally, the systematic uncertainty on column densities may arise from performance uncertainties of the *Chandra*-ACIS detector. Such uncertainties have been evaluated by Drake et al. (2006). They show that in the $10^4$ source count regime appropriate for COUP flares, instrumental uncertainties for unabsorbed ($\log N_{\rm H} \sim 20$ cm$^{-2}$) sources may become comparable to (but not exceed) statistical uncertainties. For example, their spectral simulations predict a 0.07 dex instrumental systematic error on $N_{\rm H}$, which is similar to our statistical errors of $\lesssim$0.07 dex for soft COUP sources.

[13] These are COUP stars 71, 152, 394, 597, 971, 1481, 1516, and 1595.

We thus find that the typical flare peak temperature errors shown in Figure 15*b* (typically 20%–40%) could be slightly larger (typically 25%–55%) if statistical and systematic uncertainties of $\log N_{\rm H}$ values are applied. There is no evidence that the superhot temperatures are an artifact of our analysis procedures or uncertainties. From equations (1)−(3), 25%–55% errors on peak flare temperature result in 15%–30% errors on inferred loop sizes.

As with median energies, we expect the statistical errors on COUP peak flare X-ray luminosities to be comparable to those obtained from Monte Carlo simulations of Cepheus B sources, which are $\lesssim$0.2 dex (see bottom right panel in Fig. 12 in Getman et al. 2006).

## REFERENCES


Albacete Colombo, J. F., Caramazza, M., Flaccomio, E., Micela, G., & Sciortino, S. 2007, A&A, 474, 495
Arnaud, K. A. 1996, in ASP Conf. Ser. 101, Astronomical Data Analysis Software and Systems V, ed. G. H. Jacoby & J. Barnes (San Francisco: ASP), 17
Aschwanden, M. J., & Alexander, D. 2001, Sol. Phys., 204, 91
Aschwanden, M. J., Stern, R. A., Güdel, M. 2008, ApJ, 672, 659
Beers, T. C., Flynn, K., & Gebhardt, K. 1990, AJ, 100, 32
Caramazza, M., Flaccomio, E., Micela, G., Reale, F., Wolk, S. J., & Feigelson, E. D. 2007, A&A, 471, 645
Crespo-Chacón, I., Micela, G., Reale, F., Caramazza, M., López-Santiago, J., & Pillitteri, I. 2007, A&A, 471, 929
Donati, J.-F., et al. 2007, MNRAS, 380, 1297
Drake, J. J., Ratzlaff, P., Kashyap, V., Edgar, R., Izem, R., Jerius, D., Siemiginowska, A., & Vikhlinin, A. 2006, Proc. SPIE, 6270, 49
Farnik et al. 1996, Sol. Phys., 168, 331
Favata, F., Flaccomio, E., Reale, F., Micela, G., Sciortino, S., Shang, H., Stassun, K. G., & Feigelson, E. D. 2005, ApJS, 160, 469
Feigelson, E., Townsley, L., Güdel, M., & Stassun, K. 2007, in Protostars and Planets V, ed. B. Reipurth (Tucson: Univ. Arizona Press), 313
Feigelson, E. D., et al. 2005, ApJS, 160, 379
Flaccomio, E., Micela, G., Sciortino, S., Feigelson, E. D., Herbst, W., Favata, F., Harnden, F. R., Jr., & Vrtilek, S. D. 2005, ApJS, 160, 450
Forbes, T. G., & Acton, L. W. 1996, ApJ, 459, 330
Franciosini, E., et al. 2007, A&A, 468, 485
Getman, K. V., Feigelson, E. D., Grosso, N., McCaughrean, M. J., Micela, G., Broos, P., Garmire, G., & Townsley, L. 2005a, ApJS, 160, 353
Getman, K. V., Feigelson, E. D., Townsley, L., Broos, P., Garmire, G., & Tsujimoto, M. 2006, ApJS, 163, 306
Getman, K. V., & Livshitz, M. A. 2000, Astron. Rep., 44, 255
Getman, K. V., et al. 2005b, ApJS, 160, 319
Giardino, G., Favata, F., Micela, G., & Reale, F. 2004, A&A, 413, 669
Giardino, G., Favata, F., Micela, G., Sciortino, S., & Winston, E. 2007, A&A, 463, 275
Glassgold, A. E., Feigelson, E. D., Montmerle, T., & Wolk, S. 2005, in ASP Conf. Ser. 341, Chondrites and the Protoplanetary Disk, ed. A. N. Krot, E. R. D. Scott, & B. Reipurth (San Francisco: ASP), 165
Grosso, N., Montmerle, T., Feigelson, E. D., & Forbes, T. G. 2004, A&A, 419, 653
Güdel, M. 2004, Astron. Astrophys. Rev., 12, 71
Hartmann, L. 1998, Accretion Processes in Star Formation (Cambridge: Cambridge Univ. Press)
Hiei, E. 1994, in IAU Colloq. 144, Solar Coronal Structures, ed. V. Rusin, P. Heinzel, & J.-C. Vial (Bratislava: VEDA), 163
———. 1997, Mem. Soc. Astron. Italiana, 68, 491
Hong, J., Schlegel, E. M., & Grindlay, J. E. 2004, ApJ, 614, 508
Imanishi, K., Koyama, K., & Tsuboi, Y. 2001, ApJ, 557, 747
Isobe, H., Shibata, K., Yokoyama, T., & Imanishi, K. 2003, PASJ, 55, 967
Jardine, M., Cameron, A. C., Donati, J.-F., Gregory, S. G., & Wood, K. 2006, MNRAS, 367, 917
Jardine, M., & Unruh, Y. C. 1999, A&A, 346, 883
Kahler, S. 1977, ApJ, 214, 891
Kopp, R. A., & Pneuman, G. W. 1976, Sol. Phys., 50, 85
Long, M., Romanova, M. M., & Lovelace, R. V. E. 2008, MNRAS, 386, 1274
Maggio, A., Flaccomio, E., Favata, F., Micela, G., Sciortino, S., Feigelson, E. D., & Getman, K. V. 2007, ApJ, 660, 1462
Osten, R. A., & Brown, A. 1999, ApJ, 515, 746
Osten, R. A., Drake, S., Tueller, J., Cummings, J., Perri, M., Moretti, A., & Covino, S. 2007, ApJ, 654, 1052
Pallavicini, R., Serio, S., & Vaiana, G. S. 1977, ApJ, 216, 108
Preibisch, T., et al. 2005b, ApJS, 160, 401
Priest, E. R., & Forbes, T. G. 2002, A&A Rev., 10, 313
Reale, F. 2007, A&A, 471, 271
Reale, F., Betta, R., Peres, G., Serio, S., & McTiernan, J. 1997, A&A, 325, 782
Reale, F., Güdel, M., Peres, G., & Audard, M. 2004, A&A, 416, 733
Reale, F., & Micela, G. 1998, A&A, 334, 1028
Rosner, R., Tucker, W. H., & Vaiana, G. S. 1978, ApJ, 220, 643
Serio, S., Reale, F., Jakimiec, J., Sylwester, B., & Sylwester, J. 1991, A&A, 241, 197
Shu, F. H., Najita, J. R., Shang, H., & Li, Z.-Y. 2000, in Protostars and Planets IV (Tucson: Univ. Arizona Press), 789
Shu, F. H., Shang, H., Glassgold, A. E., & Lee, T. 1997, Science, 277, 1475
Siess, L., Dufour, E., & Forestini, M. 2000, A&A, 358, 593
Stassun, K. G., van den Berg, M., Feigelson, E., & Flaccomio, E. 2006, ApJ, 649, 914
Sturrock, P. A. 1966, Nature, 211, 695
Švestka, Z., Fárník, F., Hick, P., Hudson, H. S., & Uchida, Y. 1997, Sol. Phys., 176, 355
Švestka, Z., Fárník, F., Hudson, H. S., Uchida, Y., Hick, P., & Lemen, J. R. 1995, Sol. Phys., 161, 331
Sylwester, B., Sylwester, J., Serio, S., Reale, F., Bentley, R. D., & Fludra, A. 1993, A&A, 267, 586
Testa, P., Reale, F., Garcia-Alvarez, D., & Huenemoerder, D. P. 2007, ApJ, 663, 1232
Tsuboi, Y., Koyama, K., Murakami, H., Hayashi, M., Skinner, S., & Ueno, S. 1998, ApJ, 503, 894
Wargelin, B. J., Kashyap, V. L., Drake, J. J., García-Alvarez, D., & Ratzlaff, P. W. 2008, ApJ, 676, 610
Wolk, S. J., Harnden, F. R., Jr., Flaccomio, E., Micela, G., Favata, F., Shang, H., & Feigelson, E. D. 2005, ApJS, 160, 423